

1 **Murine Parainfluenza Virus Persists in Lung Innate Immune Cells Sustaining**  
2 **Chronic Lung Pathology**

3  
4 Ítalo Araujo Castro<sup>1</sup>, Yanling Yang<sup>1</sup>, Victoria Gnazzo<sup>1</sup>, Do-Hyun Kim<sup>2</sup>, Steven J. Van  
5 Dyken<sup>2</sup>, Carolina B. López<sup>1</sup>.

6  
7 <sup>1</sup>Department of Molecular Microbiology and Center for Women's Infectious Diseases  
8 Research, Washington University School of Medicine, Saint Louis, Missouri, USA.  
9 <sup>2</sup>Department of Pathology & Immunology, Washington University School of Medicine,  
10 Saint Louis, Missouri, USA.

11  
12 **Summary**

13  
14 Respiratory viruses including the human parainfluenza viruses (hPIVs) are a constant  
15 burden to human health, with morbidity and mortality frequently increased after the acute  
16 phase of the infection. Although is proven that respiratory viruses can persist *in vitro*, the  
17 mechanisms of virus or viral products persistence, their sources, and their impact on  
18 chronic respiratory diseases *in vivo* are unknown. Here, we used Sendai virus (SeV) to  
19 model hPIV infection in mice and test whether virus persistence associates with the  
20 development of chronic lung disease. Following SeV infection, virus products were  
21 detected in lung macrophages, type 2 innate lymphoid cells (ILC2s) and dendritic cells  
22 for several weeks after the infectious virus was cleared. Cells containing viral protein  
23 showed strong upregulation of antiviral and type 2 inflammation-related genes that

24 associate with the development of chronic post-viral lung diseases, including asthma.  
25 Lineage tracing of infected cells or cells derived from infected cells suggests that distinct  
26 functional groups of cells contribute to the chronic pathology. Importantly, targeted  
27 ablation of infected cells or those derived from infected cells significantly ameliorated  
28 chronic lung disease. Overall, we identified persistent infection of innate immune cells as  
29 a critical factor in the progression from acute to chronic post viral respiratory disease.

30

### 31 **Introduction**

32

33 Infections with respiratory RNA viruses pose a constant threat to human health. It  
34 is estimated that Respiratory Syncytial Virus (RSV) alone is associated with more than  
35 149,000 fatal cases of lower respiratory tract infection worldwide every year<sup>1</sup>. Among  
36 paramyxoviruses, human metapneumovirus (hMPV) is responsible for approximately  
37 643,000 hospitalizations and >16,000 deaths globally<sup>2</sup> every year, while hPIV accounts  
38 for 725,000 hospitalizations and >34,000 deaths<sup>2,3</sup>. Within the pediatric population, acute  
39 lower respiratory infections of viral etiology remain the leading cause of mortality in the  
40 absence of a pandemic<sup>4,5</sup>.

41 In addition to the public health burden, acute respiratory viral infections at an early  
42 age are associated with the development of chronic lung diseases including asthma and  
43 chronic obstructive pulmonary disease (COPD), while infections later in life can lead to  
44 severe exacerbations of these conditions<sup>6,7</sup>. Influenza, RSV, hMPV, hPIV, and rhinovirus  
45 infections have been linked to development and progression of COPD and lung fibrosis

46 in humans, and more recently SARS-CoV-2 infection was implicated in chronic lung  
47 diseases<sup>8-10</sup>.

48 It has been long established that RNA viruses can persist in humans. The best  
49 studied example is measles virus that persists in the central nervous system of patients  
50 with subacute sclerosing panencephalitis<sup>11,12</sup>. Other examples include Ebola virus  
51 persistence in the testis<sup>13</sup> and chikungunya virus persistence in the joints<sup>14</sup>. In addition,  
52 accumulating evidence suggests that respiratory viruses can establish persistent  
53 infections in the lung<sup>15-17</sup>. A comprehensive screening of post-mortem tissue from fatal  
54 COVID-19 cases indicated presence of viral proteins, viral RNA, and infectious SARS-  
55 CoV-2 in the respiratory tract and other anatomical sites for longer than 30 days after  
56 symptom onset<sup>15</sup>. Prolonged viral shedding has been reported in stem cell transplant  
57 recipient patients<sup>18</sup> and immunocompromised patients infected with hPIV<sup>16,18</sup>. In addition,  
58 high detection rates of hPIV3 in turbinate epithelial cells were reported in patients  
59 suffering from post-viral olfactory dysfunction<sup>19</sup>. Prolonged exposure to viral RNA and  
60 antigens, even in the absence of infectious viral particles, can work as immune stimulation  
61 factors and contribute to chronic inflammation<sup>20,21</sup>. Therefore, it is critical to better  
62 understand the mechanisms of virus or viral products persistence, the sources of the  
63 virus, and their impact on chronic respiratory diseases.

64 Here, we used respiratory infection with the murine paramyxovirus Sendai (SeV;  
65 recently renamed Murine respirovirus) to model hPIV infections in mice and study the  
66 persistence of virus and viral products and their impact on chronic lung disease. We show  
67 that viral antigens and RNA are present in specific innate immune cells populations in the  
68 lung long after the acute infection has been cleared. Importantly, we demonstrate that

69 infected cells, as well as cells derived from infected cells, play critical roles in maintaining  
70 post-viral chronic lung pathology.

71

72 **Results**

73

74 **Severe SeV lower respiratory tract infection leads to long term persistence of viral**  
75 **protein and RNA in the lung.**

76 To evaluate whether mouse parainfluenza viruses persist in the respiratory tract,  
77 we infected mice intranasally with a sublethal dose of SeV strain 52 that induced severe  
78 respiratory disease, as we and others have described previously<sup>22,23</sup>. We monitored  
79 disease progression from 3 to 49 days post-infection (dpi), analyzing virus load and  
80 presence of virus proteins in the lungs at these time points (**Figure 1A**). Day 49 post  
81 infection has been established as a standard timepoint to study post-SeV chronic lung  
82 disease as pathology has plateaued by then<sup>24</sup>. Acute weight loss following SeV infection  
83 was maximal between days 7 and 8 post-infection, with animals losing about 25% of their  
84 original weight (**Figure 1B**). All mice fully recovered their weights by day 35 post-infection.  
85 As expected, virus RNA and infectious particles were detected in whole lung  
86 homogenates on day 3 post-infection, however, only viral RNA was detected on day 49  
87 post-infection (**Figure 1C**). Immunofluorescence analysis for SeV nucleoprotein (NP) and  
88 RNAscope analysis for NP RNA (mRNA and genomic RNA) revealed a different  
89 distribution of NP in the acute and chronic phases of the infection. While NP was mostly  
90 detected in the airways lining epithelium on 3 dpi, SeV positive signal on day 49 post-

91 infection was mostly found in the alveolar compartment associated with infiltrating cells  
92 (**Figure 1D**).

93 The chronic pulmonary disease caused by SeV was marked by intense tissue  
94 remodeling, with expansion of basal epithelial cells (Krt5<sup>+</sup>) in well-delimited lesions. It was  
95 noticeable that cells persistently expressing viral NP were adjacent to Krt5<sup>+</sup> lesions,  
96 frequently organized in patches (**Figure 1E, subpanels E1-3**), while no NP<sup>+</sup> cells were  
97 found in the unaffected areas of the lung (**Figure 1E, subpanel E4**). Overall, these  
98 observations demonstrate that viral RNA and viral proteins are detectable in the chronic  
99 phase of the infection, weeks after infectious virus has been cleared<sup>23</sup>, and indicate that  
100 there is a differential distribution of virus-infected cells in the lung during the acute (day  
101 3) and chronic (day 49) phases of the infection.

102

103 **Persistent SeV proteins are detected in type 2 innate lymphoid cells (ILC2s),**  
104 **macrophages and dendritic cells.**

105 Given the diversity of cells that compose the lung inflammatory microenvironment  
106 during SeV-driven chronic disease and that most of the persistent SeV NP<sup>+</sup> cells were  
107 in the alveolar compartment (**Figure 1D, E**), we hypothesized that the persistent NP  
108 signal was mostly related to resident and infiltrating immune cells. We then used a panel  
109 of markers representing cell types frequently found in SeV-driven infiltrates in mouse  
110 lungs to characterize SeV NP<sup>+</sup> cells by immunofluorescence and flow cytometry. Initially,  
111 after using antibodies against CD3 (T lymphocytes), CD11c and CD11b (dendritic cells -  
112 DCs), F4/80 (macrophages) and Thy1.2 (T cells and ILCs), we observed that CD11c<sup>+</sup>,  
113 CD11c<sup>+</sup>CD11b<sup>+</sup>, F4/80<sup>+</sup> and CD3-Thy1.2<sup>+</sup> cells were found to be positive for SeV NP in

114 lung sections from 49 dpi (**Figure 2A**). Myeloid- cells, CD11c<sup>+</sup>, CD11b<sup>+</sup> and double-  
115 positive cells, likely DCs (**Figure 2A-a1**) and macrophages (**Figure 2A-a2**), were found  
116 frequently co-expressing SeV NP, either diffusely dispersed through the lung section or  
117 clustered surrounding blood and lymphatic vessels. Unexpectedly, SeV NP signal was  
118 also detected in CD3-Thy1.2<sup>+</sup> cells in a considerably high frequency (**Figure 2A-a3**).

119 To quantify and better characterize the cell subtypes that are sources of persistent  
120 virus antigens, we employed multiplex spectrum flow cytometry to analyze SeV-infected  
121 mouse lungs at the chronic stage of the infection (**Figure S1**). Single-cell suspensions  
122 obtained from acute SeV infection yielded on average  $13.8 \pm 2.9\%$  live, NP<sup>+</sup> cells. On day  
123 49 after infection, the percentage of live NP<sup>+</sup> cells was  $2.12 \pm 0.7\%$  (representative dot  
124 plots in **Figure 2B** and quantitative analysis in **Figure 2C**). We then analyzed individual  
125 cell subtypes to determine the percentage of SeV NP<sup>+</sup> cells within each subset. Amongst  
126 lymphoid-origin cells, ILC2s displayed the highest percentages and MFI of NP expression  
127 ( $15.7 \pm 3.5\%$ ) (**Figure 2D** and **E**, left panels). Meanwhile, tissue macrophages (TMs)  
128 ( $12.01 \pm 1.3\%$ ) and DCs ( $8.65 \pm 3\%$ ) were the myeloid subsets with the highest percentages  
129 of NP signal among the cell types analyzed (**Figure 2D** and **E**, right panels). Altogether,  
130 our data strongly indicate that macrophages, ILC2s and dendritic cells are the main  
131 sources of persistent virus antigens during chronic SeV infection.

132

133 **Innate immune cells sustain type 2-inflammation during SeV-driven chronic lung**  
134 **disease.**

135 Macrophages, dendritic cells and ILC2s participate in the establishment of chronic  
136 lung disease upon SeV infection through the IL-33/IL-13 axis<sup>25</sup>. Finding these cells

137 harboring persistent viral products raised additional questions about their impact on the  
138 pathogenesis of chronic lung disease. We sorted ILC2s and macrophages from SeV-  
139 infected IL-13 reporter (sm13)<sup>26,27</sup> mouse lungs at 49 dpi and analyzed their  
140 transcriptomic signatures against mock-infected animals to characterize their activation  
141 state. ILC2s displayed a total of 732 differentially expressed genes (DEGs) over mock,  
142 with 276 being upregulated and 456 being downregulated (P<0.05 and LogFC>2) (**Figure**  
143 **3A**). We observed a significant increase of ILC2 hallmark genes<sup>28</sup>, including *Gata3*, *Rora*,  
144 *IL5*, *IL13*, *Areg*, *Klrg1*, and *Il1rl1* (ST2) (**Figure 3B**), as well as genes known to be  
145 increased in the context of RNA virus infection (**Figure 3C**). Gene set enrichment analysis  
146 (GSEA) showed that lung ILC2s from SeV-infected were enriched in pathways previously  
147 linked to SeV infection<sup>29</sup>, including the TNFR2 non-canonical NF- $\kappa$ B pathway (**Figure**  
148 **3G**). Moreover, DEGs from sorted ILC2s show signatures associated with type 2 immune  
149 responses and inflammation, supporting the role of ILC2s in maintaining the chronic type  
150 2 immunopathology observed in SeV-infected lungs at 49 dpi (**Figure 3G**). Lung  
151 macrophages from SeV-infected mice displayed 478 upregulated DEGs compared to  
152 mock (**Figure 3D**), from which classical genes involved in Th2 inflammation<sup>30</sup>, including  
153 *Arg1*, *Chil3*, *Ccl11*, *Il1rl1* (ST2), and *Il33* were significantly increased (**Figure 3E**). In  
154 addition, these macrophages had transcriptomic signatures associated to increased  
155 phagocytic activity<sup>31</sup> such as *Cd63*, *Cd68*, and *Fcgr2b* (**Figure 3F**). Similar to what was  
156 shown for ILC2s, upregulated genes in macrophages were enriched in GSEA signatures  
157 directly involved in chronic lung disease (**Figure 3G**). These findings indicated that innate  
158 immune cells display a strong gene expression polarization towards type 2 inflammatory  
159 responses and show transcriptomic footprints that are indicative of virus infection and

160 chronic lung diseases, confirming their involvement in the pathogenesis of post-viral  
161 chronic lung disease.

162

163 **Virus-infected cells and/or cells derived from them contribute to the chronic**  
164 **inflammatory state following SeV infection.**

165 Long-term exposure to viral antigens and RNA in the respiratory tract is likely to  
166 have important implications on the tissue microenvironment. To directly evaluate the  
167 transcriptome of persistently infected cells, we generated a double-reporter virus by  
168 inserting an eGFP and a Cre recombinase as independent genes between the N and the  
169 P genes of the SeV Cantell strain (rSeV-C<sup>eGFP-Cre</sup>) (**Figure S2A**). We then used rSeV-  
170 C<sup>eGFP-Cre</sup> to infect tdTomato reporter mice that contain a Cre reporter allele flanked by  
171 loxP-STOP cassettes (**Figure S2B**). We harvested lungs on day 49 pi for flow cytometry  
172 and FACS analysis (**Figure 4A**). Infection with rSeV-C<sup>eGFP-Cre</sup> progressed in a similar way  
173 as our previously described SeV-52 model. Weight loss of up to 20% of the original weight  
174 was observed until day 9 post-infection, with steady recovery until no differences from  
175 uninfected animals by day 21 (**Figure 4A**). Upon transcription of the viral genome, Cre is  
176 expressed and excises the loxP-STOP cassette that blocks the tdTomato gene construct  
177 leading to expression of the reporter. Virus-infected cells, cells that cleared the infection  
178 in a non-cytolytic manner, and cells derived from these cells will have constitutive  
179 expression of the tdTomato fluorescent protein (tdTom) (**Figure S2B**). At 3 dpi, the  
180 frequency of tdTom<sup>+</sup> cells in infected lungs was 21.3% $\pm$ 0.6%, and this number decreased  
181 to 10 $\pm$ 2.6% at 49 dpi (**Figure 4B-C**, includes a representative sample). From these cells,  
182 at 3 dpi 84.4% $\pm$ 3.8% were characterized as non-immune (CD45<sup>-</sup>) and 15.4% $\pm$ 3.8% were

183 characterized as immune cells (CD45<sup>+</sup>) (**Figure 4D-E**, includes a representative sample),  
184 similar to what we observe during SeV-52 acute infections. The proportion of non-immune  
185 tdTom<sup>+</sup> cells at 49 dpi remained high (90.9%±0.3%) and immune cells accounted for  
186 8.8%±0.2% of all tdTom<sup>+</sup> events (**Figure 4D-E**, includes a representative sample). As  
187 previously reported, the constitutive expression of tdTomato upon Cre exposure is  
188 independent of further viral replication, and all tdTom<sup>+</sup> cells, even those that cleared the  
189 infection would express the reporter protein<sup>32</sup>. To differentiate cells persistently  
190 expressing viral protein from all other tdTom<sup>+</sup> cells, we combined tdTom detection with  
191 SeV NP staining. Using this strategy, we identified three distinct cell populations in tdTom  
192 reporter mice on day 49 after infection with rSeV-C<sup>e</sup>GFP-Cre: tdTom<sup>+</sup>NP<sup>-</sup>, tdTom<sup>+</sup>NP<sup>+</sup>, and  
193 negative cells (**Figure 4F**). We then sorted these populations for transcriptome analysis.  
194 To increase RNA yields, we used three pools of two individual infected animals for sorting.  
195 In addition, we obtained negative cells from mock-infected tdTom reporter animals as  
196 controls. The samples were subjected to total RNA-seq. We found reads mapping to the  
197 viral genome or the eGFP reporter gene in all three tdTom<sup>+</sup>NP<sup>-</sup> cell pools and in all three  
198 tdTom<sup>+</sup>NP<sup>+</sup> pools (**Figure 4G**). Alignment to the rSeV-C<sup>e</sup>GFP-Cre genome showed viral  
199 reads mapping to multiple viral genes, including the polymerase L gene in some of the  
200 pools (**Figure H**), confirming that tdTom<sup>+</sup>NP<sup>-</sup> cells have been exposed to the virus either  
201 by direct infection or through their progenitors.

202 After identifying two major cell subsets relevant to virus-host interactions in  
203 persistent SeV infection, we sought to understand their role in pathogenesis by comparing  
204 the host transcriptomic profiles of tdTom<sup>+</sup>NP<sup>-</sup> and tdTom<sup>+</sup>NP<sup>+</sup> cells. Transcriptomic  
205 analysis of the different pools showed differentially expressed genes (DEGs) in

206 tdTom<sup>+</sup>NP<sup>-</sup> and tdTom<sup>+</sup>NP<sup>+</sup> cells over mock (**Figure 5A**) ( $p < 0.05$  and  $\text{LogFC} > 2$ ). Negative  
207 cells showed no significant transcriptomic changes over mock (**Figure 5A**), suggesting  
208 that only direct virus-host interactions lead to long-term host gene expression changes,  
209 rather than a more widespread effect to non-infected cells in the lung.

210 From the identified DEGs, 2376 were exclusive of tdTom<sup>+</sup>NP<sup>-</sup> and 387 DEGs were  
211 exclusive of tdTom<sup>+</sup>NP<sup>+</sup> cells (**Figure 5B**). Gene Ontology (GO) analysis indicated that  
212 tdTom<sup>+</sup>NP<sup>-</sup> cells have gene expression signatures associated to extracellular matrix  
213 organization, epithelial cell migration, wound healing, lung epithelial cell differentiation,  
214 tissue remodeling and keratinocyte proliferation (**Figure 5C**), of note, the extracellular  
215 matrix organization factors *Col1a1*, *Col3a1*, *Col5a1*, and *Fbln1*, and the cell proliferation  
216 factors *Cd34*, *Tgfb3*, *Cldn1*, *Egfr*, and *Fgf10*, all included in the wound healing pathway  
217 (**Figure 5D**).

218 Differently, tdTom<sup>+</sup>NP<sup>+</sup> DEGs included genes associated with mononuclear cell  
219 proliferation and migration, response to virus, positive regulation of inflammatory  
220 response, lymphocyte activation, and innate immune response (**Figure 5C**). Genes  
221 involved in lymphocyte activation and proliferation included *Cd44*, *Itgb2*, *Cd274*, *Cd2*, and  
222 *Card11*. Among genes involved in positive regulation of innate immune responses, *Cd68*,  
223 *Chil3*, *Fcgr3*, *Fcer1g* and *Fcgr1* are examples of myeloid-related genes, *Gata3*, and *Thy1*  
224 are examples of innate lymphoid-related genes (**Figure 5D**), and *Il33* is a known gene  
225 involved in Type-2 immunopathology<sup>22</sup>.

226 Gene set enrichment analysis (GSEA) comparing tdTom<sup>+</sup>NP<sup>-</sup> and tdTom<sup>+</sup>NP<sup>+</sup> cell  
227 transcriptomes confirmed the distinct transcriptomes of these cell populations. Survivor  
228 tdTom<sup>+</sup>NP<sup>-</sup> cells had enriched signatures associated to tissue remodeling, keratinization,

229 and tissue homeostasis-related pathways (**Figure 5E**). On the other hand, persistent  
230  $\text{tdTom}^+\text{NP}^+$  cells had enriched signatures mapping almost exclusively to immune and  
231 inflammation-related pathways, such as myeloid cell development, innate immunity, lung  
232 cancer, and oxidative phosphorylation (**Figure 5E**). These observations indicate that  
233 while cells that cleared SeV infection initiate and maintain a transcriptomic program to  
234 control inflammation and to resolve lung injury, cells persistently exposed to viral products  
235 have a pro-inflammatory profile with potential implications on lung pathogenesis.

236

237 **Persistent infected cells and its progeny are directly involved in the progression of**  
238 **chronic lung disease.**

239 We next set out to investigate the impact of persistent infected cells in the lung  
240 chronic disease progression. To do this, we combined our rSeV-C<sup>eGFP-Cre</sup> with Cre-  
241 inducible Diphtheria toxin receptor (iDTR) mice<sup>33</sup>, where SeV-infected cells constitutively  
242 express DTR. DTR-expressing cells would then be susceptible to specific ablation  
243 following DT administration. We then intranasally injected the iDTR mice with either PBS  
244 (mock) or  $2 \times 10^5$  TCID<sub>50</sub>/animal of rSeV-C<sup>eGFP-Cre</sup>, treated with two consecutive doses of  
245 DT, and analyzed their lungs by flow cytometry at 5 dpi to check for depletion of infected  
246 cells (**Figure S3A**). The DT treatment did not impact disease progression, and both  
247 infected groups lost up to 20% of their original weight and recovered thereafter (**Figure**  
248 **6B**). Flow cytometry quantification of SeV NP<sup>+</sup> cells indicated that two consecutive DT  
249 doses were sufficient to deplete more than 80% of infected cells (**Figure S3B-C**) as  
250 described previously<sup>33</sup>. To deplete persistent infected cells, we waited until 21 dpi to avoid  
251 the acute and clearance phases of SeV infection and used the same 2-dose DT regime,

252 with the final time point for analysis at 49 dpi (**Figure 6A**). Infected groups showed the  
253 typical signs of disease progression following SeV infection, and the DT regime did not  
254 cause weight loss in the 5 days following intraperitoneal administration (**Figure 6B**). As  
255 expected, infected mice that were not treated with DT had the typical signs of chronic lung  
256 disease caused by SeV, including alveolitis, bronchiolization of the alveolar compartment,  
257 and bronchoalveolar lymphoid tissue (BALT) formation<sup>22</sup> (**Figure 6C**). Noticeably, DT-  
258 mediated ablation of persistently infected and survivor cells decreased the intensity of the  
259 lung disease (**Figure 6C-D**), and lung sections displayed minimal pathology compared  
260 with untreated controls. Targeted DT ablation of SeV NP<sup>+</sup> cells also significantly  
261 decreased the area affected by chronic lesions, marked by intense agglomeration of basal  
262 stem cells (Krt5<sup>+</sup>) and transitory epithelial cells (Krt8<sup>+</sup>) (**Figure 6E-F**), hence  
263 demonstrating that persistent infected cells and its progeny are directly involved in the  
264 progression of SeV-driven chronic lung disease.

265

## 266 **Discussion**

267 RNA virus-host interactions are proving more complex and intricated than they  
268 were thought to be. Increasing evidence shows that a diversity of RNA viruses can remain  
269 in their host in different forms past acute illness recovery, clearance of infectious viral  
270 particles and development of specific immunity, resulting in harmful long-term clinical  
271 manifestations with epidemiological implications<sup>20,34,35</sup>. Frequently, persistent RNA  
272 infections are found in very specific niches, for instance, the CNS, testis, ocular tissue,  
273 and secondary lymphoid organs. Here, using a natural host-pathogen model, we describe  
274 the implications of respiratory virus persistence in a non-canonical immune privileged site,

275 the lower respiratory tract. In accordance to previous reports for SARS-CoV2 and  
276 influenza virus<sup>17,36</sup>, we showed detection not only of SeV RNA from multiple viral genes  
277 for up to 49 dpi, but also of viral antigens, indicating that some level of persistent viral  
278 RNA translation is still in place during the persistent phase of the infection, even with  
279 undetectable infectious viral particles. Importantly, we identified ILC2, macrophages and  
280 dendritic cells as the main cells harboring persistent viral products in the lung, and we  
281 demonstrate that depletion of cells that have been directly infected or those derived from  
282 infected cells significantly reduce chronic post-viral lung disease.

283 Our data indicate that between the early stages of SeV infection and the later  
284 chronic lung inflammation there is a major shift of viral antigen and RNA cell sources  
285 (**Figures 1 and 2**). As expected, based on previous reports<sup>37</sup> airway cells were the major  
286 source of viral proteins and RNA on day 3 post-SeV infection. However, on day 49 post-  
287 infection cells in the alveolar compartment were the sources of viral products, with no  
288 detectable virus RNA nor antigens in epithelial cells. Upon immunofluorescence and flow  
289 cytometry, these viral product sources were characterized as dendritic cells,  
290 macrophages and ILC2s. One of the hallmarks of the chronic SeV-driven  
291 immunopathology is the increased number of alternatively activated macrophages  
292 (AAMs) and monocyte-derived dendritic cells in infected mouse lungs<sup>38-40</sup>. These cells  
293 were shown to partner with ILC2s, also found in increased numbers in this condition,  
294 contributing to chronic type 2 inflammation in an IL-33/IL-13 axis-dependent manner<sup>25</sup>. In  
295 light of our findings, we hypothesize that immune cells with phagocytic activity, such as  
296 macrophages and dendritic cells, interact with SeV-infected epithelial cells and become  
297 sources of viral RNA and protein, as previously shown that macrophages and dendritic

298 cells remain positive for SeV RNA by qPCR for up to 21 dpi<sup>40</sup>. The transcriptomic  
299 signatures of sorted macrophages during SeV chronic lung disease support these  
300 observations, with strong Th2 polarization and increased expression of phagocytic  
301 activity-related genes (**Figure 3**), but no significant changes in markers suggestive of  
302 active viral infection (data not shown).

303 For the myeloid compartment, phagocytosis of viral-infected cells is a known  
304 pathway whereby professional phagocytes could acquire viral antigens and even become  
305 infected. Unexpectedly, we found ILC2s as one of the most significant sources of  
306 persistent viral subproducts following SeV infection. Since ILC2s lack phagocytic activity,  
307 our results suggest that expression of SeV antigens is a consequence of viral infection.  
308 ILC2s from SeV persistently infected lungs displayed upregulated ILC2 hallmark IL-2-  
309 STAT5 and Th2 inflammation genes, corroborating previous studies covering ILC2 roles  
310 in post-viral respiratory disease<sup>28,41</sup>. However, we also reported genes upregulated during  
311 viral infection, such as *Ifitm1* and *Traf1*, involved in viral infection response pathways. To  
312 the best of our knowledge, this is the first report demonstrating the persistent expression  
313 of viral antigens in innate lymphoid cells.

314 Typical infections caused by highly cytopathic viruses were thought to follow a  
315 canonical chain of events culminating with cell lysis, tissue damage, release of pro-  
316 inflammatory mediators, and viral clearance. Nonetheless, it was recently shown that cells  
317 can overcome viral infection in a non-lytic way and either the infected surviving cell or its  
318 daughter cells have diverse long-term implications<sup>42-46</sup>. For instance, influenza A virus  
319 (IAV)-directly infected or derived from infected club cells showed a pro-inflammatory  
320 profile that implicated in lung pathology in mice<sup>42</sup>, while also exerting a protective role

321 against secondary infections<sup>43</sup>. Survivor epithelial cells from another respiratory  
322 orthomyxovirus infection, influenza B virus (IBV), were also shown to be critical to  
323 maintain respiratory barrier function in a murine model of IBV infection<sup>45</sup>. The infection by  
324 SeV, a murine respirovirus, also left a significant percentage of survivor cells in mouse  
325 lungs, from which the majority were epithelial cells (**Figure 4**). Interestingly, even as early  
326 as 3 dpi, CD45<sup>+</sup> immune cells were positive for the reporter tdTom, indicating active viral  
327 replication or phagocytosis of infected cells. After 49 days of the infection, CD45<sup>+</sup> immune  
328 cells were still part of the tdTom<sup>+</sup> cell pool, suggesting that for paramyxoviruses the  
329 diversity of survivor cells goes beyond the epithelial compartment.

330 As suggested previously, survivor cells could act as long-term sources of viral  
331 antigens<sup>47</sup> with potential role in chronic lung disease development and lung healing. We  
332 successfully combined the cell-fate tracing system using Cre-dependent tdTom reporter  
333 mice/rSeV-C<sup>eGFP-Cre</sup> with virus antigen detection to better characterize survivor and virus  
334 persistent cells. For both survivor cells with or without persistent expression of SeV NP  
335 (tdTom<sup>+</sup>NP<sup>-</sup> and tdTom<sup>+</sup>NP<sup>+</sup>), SeV RNA was detected and coverage analysis after  
336 RNAseq indicated multiple viral genes represented, including the polymerase L gene,  
337 suggestive of low replicative levels in SeV persistent cells. Based in our previous cell  
338 characterization of persistent SeV-antigen expressing cells, we hypothesized that the  
339 survivor tdTom<sup>+</sup>NP<sup>+</sup> cells were exclusively immune cells.

340 Cells that manage to survive a non-cytolytic clearance of RNA viruses after the  
341 acute stages of the infection can maintain abnormal transcriptomic footprints for weeks<sup>46</sup>.  
342 After following SeV-infected mice for a long-term post-infection (49 dpi) but also keeping  
343 in mind that the chronic lung disease is present at this timepoint, we assessed the

344 transcriptomic signatures of tdTom<sup>+</sup> cells in comparison with negative and mock cells.  
345 Surprisingly, deep transcriptomic changes were observed only in survivor tdTom<sup>+</sup>NP<sup>-</sup> and  
346 tdTom<sup>+</sup>NP<sup>+</sup> cells. Negative cell transcriptomes resembled mock cells, giving no significant  
347 differentially expressed genes. A similar observation was made with uninfected cells from  
348 IBV infected mice at 14 days in comparison with their correspondent controls<sup>45</sup>. These  
349 findings indicate that at later stages of paramyxovirus infection, the lung transcriptomic  
350 changes are a result of direct virus-cell interaction events and not due to responses to  
351 secondary secreted mediators. Given the diversity of survivor cells that we described from  
352 a respiratory paramyxovirus infection, we expected correspondent diverse roles in  
353 pathogenesis. We observed that tdTom<sup>+</sup>NP<sup>-</sup> cells presented gene expression signatures  
354 matching to tissue remodeling, wound healing, and lung regeneration pathways, typically  
355 seen in survival epithelial cells from respiratory orthomyxovirus infections<sup>42,45</sup>. However,  
356 infected cells expressing persistent SeV antigens (tdTom<sup>+</sup>NP<sup>+</sup> cells) displayed a different  
357 gene signature enriched in proinflammatory genes, matching the gene expression profiles  
358 we described from sorted innate immune cells from SeV-driven chronic lung disease.

359 To address the impact of SeV-survivor cells in the subsequent chronic lung  
360 pathology, we employed Cre-inducible diphtheria toxin receptor (iDTR) mice in  
361 combination with our rSeV-C<sup>e</sup>GFP-C<sup>re</sup> virus and performed DT-mediated ablation of viral  
362 infected cells and its progeny way after the timepoints were SeV infection is considered  
363 cleared. Unfortunately, we were not able to specifically deplete persistent SeV-survivor  
364 NP<sup>-</sup> or NP<sup>+</sup> cell populations one at a time at this point due to lack of appropriate tools  
365 available to us. Regardless of the fact that DT ablation affects all DTR-expressing  
366 populations (persistent infected, virus-cleared, and its progeny), and not only the survivor

367 NP<sup>+</sup> cells, there was a significant impact on pathogenesis, reinforcing that the chronic  
368 Th2-biased inflammation induced by survivor SeV NP<sup>+</sup> cells is a key factor to the  
369 maintenance of the “post-viral” chronic lung disease.

370 In summary, our study demonstrates that paramyxovirus RNA and antigens persist  
371 in the lower respiratory tract associated with innate immune cells for months after the viral  
372 infection is thought to be cleared. More importantly, clearance of SeV infection is not  
373 complete, leaving a complex collection of survivor cells including epithelial and immune  
374 cells, each carrying distinct transcriptomic signatures. Long-term expression of virus  
375 antigens by survivor cells was proven to be a key factor for the immunopathology of  
376 paramyxovirus infection as a persistent source of activation for innate immune cells,  
377 which leads to maintenance of the robust type 2 environment in the SeV-driven chronic  
378 lung disease. Our data not only shed light into the cellular fate following respiratory  
379 infections and its long-term implications on chronic disease, but also pave the road for  
380 studies to further characterize the functions of persistent virus antigen-expressing cells  
381 and designing antiviral strategies.

382

### 383 **Materials and Methods**

384

#### 385 **Mice, Virus Infection and Virus Titration**

386 Seven- to 9-weeks old female wt C57BL/6 mice were either bred in house or purchased  
387 from Taconic Biosciences (Rensselaer, NY). B6.Cg-Gt(ROSA)26Sor<sup>tm14(CAG-tdTomato)Hze</sup>/J  
388 (tdTomato) and C57BL/6-Gt(ROSA)26Sor<sup>tm1(HBEGF)Awai</sup>/J (iDTR) mice were either bred in  
389 house or purchased from The Jackson Laboratory. B6.129S4(C)-II13<sup>tm2.1Lky</sup>/J (sm13)

390 mice were previously described<sup>26,27</sup> and bred at Washington University in St. Louis.  
391 Sendai virus strain 52 (SeV-52) stocks were expanded in 10-days-old embryonated  
392 chicken eggs (Charles River Laboratories, Wilmington, MA) and virus titers were  
393 determined using end-point dilution tissue culture infectious dose (TCID<sub>50</sub>) infectivity  
394 assays<sup>48</sup> in LLC-MK2 cells. For mice infections, animals were anesthetized with standard  
395 doses of Xylazine/Ketamine and injected intranasally with 40 µL of either PBS or diluted  
396 virus to a final dose of 5x10<sup>4</sup> TCID<sub>50</sub> for SeV-52 or 5x10<sup>5</sup> TCID<sub>50</sub> for rSeV-C<sup>eGFP-Cre</sup>,  
397 corresponding to 10 times the virus ID50 ensuring that all mice were infected. Mouse  
398 groups were then monitored for weight loss as an indicator of disease progression for up  
399 to 49 dpi. To obtain lung viral titers, lung lobes were homogenized in 0.1% Gelatin,  
400 clarified by centrifugation, and analyzed by infectivity assays in LLC-MK2 cells. iDTR mice  
401 were administered with 100 ng of Diphtheria toxin (DT) (Sigma) intraperitoneally at days  
402 3 and 4 for depletion of rSeV-C<sup>eGFP-Cre</sup>-infected cells. To achieve depletion of persistently  
403 infected and survivor cells, DT treatment was performed at days 21 and 22 post-infection.  
404

405 **Generation of rSeV-C<sup>eGFP-Cre</sup>**

406 The full-length SeV Cantell viral antigenome sequence (NCBI accession number  
407 OR764764) was inserted into the pSL1180 vector flanked at the 5' by the T7 polymerase  
408 promoter and a Hammer-head Ribozyme (Hh-Rbz) and at the 3' by a second Ribozyme,  
409 and the T7 terminator. The reporter eGFP and the recombinase Cre genes were inserted  
410 as independent reading frames between the virus genes N and P, flanked by the  
411 duplicated N/P intergenic region. A NotI restriction site was inserted after the eGFP gene,  
412 as well as 4 nucleotides after the Cre gene to ensure the whole genome would meet the

413 paramyxovirus “rule of six”. Three helper plasmids were made by cloning NP, P, and L  
414 genes of SeV Cantell into the pTM1 vector. All these plasmids were confirmed by  
415 nanopore sequencing.

416 To rescue the recombinant virus, BSR-T7 cells grown in DMEM containing 10%  
417 FBS, 50ng/mL Gentamicin, 1mM Sodium Pyruvate, and 2mM L-Glutamine were  
418 transfected with a plasmid’s mixture containing 4.0 µg pSL1180- rSeV-C<sup>eGFP-Cre</sup> 1.44 µg  
419 pTM1-NP, 0.77 µg pTM1-P and 0.07 µg pTM1-L using Lipofectamine LTX according to  
420 manufacturer’s guidelines. After a 5 h incubation, the medium was changed to infection  
421 medium (DMEM containing Pen/Strep, 35% Bovine Serum Albumin (BSA) (Sigma), 5%  
422 NaHCO<sub>3</sub>) with 1 µg/mL TPCK-treated trypsin (Worthington Biochem. Corporation), then  
423 cells were incubated at 37°C. The monolayers were monitored daily for eGFP expression  
424 and harvested on day 4 post-transfection. After 3 freeze-thaw cycles, the supernatants  
425 were clarified by centrifugation and used to infect 10-day-old embryonated chicken eggs  
426 through the allantoic cavity. After incubation for 40 hours at 37°C, 40 – 70% humidity, the  
427 allantoic fluids were harvested and the TCID<sub>50</sub> was measured using LLC-MK2 cells.

428

#### 429 **RNA extraction and RT-qPCR**

430 Lung samples were homogenized in TRIzol (Ambion Inc.), and total RNA was extracted  
431 following manufacturer’s guidelines. To remove any trace of DNA contaminants, 1 µg of  
432 total RNA was treated with DNase I (Thermo scientific) following manufacturer’s  
433 guidelines and cDNA synthesis was then carried out with the High-Capacity cDNA  
434 Reverse Transcription kit (Applied biosystems). For quantitative analysis by RT-PCR  
435 (qPCR), 10 ng/µL of cDNA was amplified using SYBR Green Mastermix (Thermofisher)

436 in a BioRad C1000 Touch thermal cycler (BioRad). SeV NP (forward 5-  
437 TGCCCTGGAAGATGAGTTAG-3', reverse 5'-GCCTGTTGGTTGTGGTAAG-3')  
438 relative copy numbers were normalized to mouse GAPDH (forward 5-  
439 CTCCCACCTCCACCTTCG-3', reverse 5'-CCACCACCCCTGTTGCTGTAG-3') and  
440 corrected for mouse alpha-Tubulin (forward 5'-TGCCTTGTCACGGTATG-3', reverse  
441 5'-CTGGAGCAGTTGACGACAC-3') expression as described previously<sup>22</sup>.

442

443 **Generation of recombinant huFc-SeV NP antibody**

444 Sequence of the mouse variable heavy and kappa chains were obtained by using  
445 SMARTer 5' RACE technology (Takara Bio, USA) adapted for antibodies to amplify the  
446 variable genes from heavy and kappa chains for each hybridoma based on isotype.  
447 Briefly, RNA was extracted from each hybridoma using Qiagen RNeasy Mini Kit (Qiagen,  
448 Valencia, CA), followed by first stand cDNA synthesis using constant gene specific 3'  
449 primers (GSP) based on the specific isotype of the hybridoma and incubation with the  
450 SMARTer II A Oligonucleotide and SMARTscribe reverse transcriptrase. Amplifying PCR  
451 of the first stand cDNA product was then performed using SeqAmp DNA  
452 Polymerase (Takara) with a nested 3' primer to the constant genes and a 5' universal  
453 primer based on universal primer sites added to the 5' end during cDNA generation.  
454 Purified PCR product was then submitted for Sanger sequencing using 3' constant gene  
455 primers (GeneWiz, South Plainfield, NJ). Sequence results were blasted against the  
456 IMGT human databank of germline genes using V-Quest (<http://imgt.org>) and analyzed  
457 for CDR3/junction identity and V(D)J usage. Clones were chosen from each clonal family,  
458 and DNA was synthesized and cloned in-framed into pcDNA3.4 vector containing a

459 human IgG1 constant region and a human kappa light chain constant region, making a  
460 chimeric mouse variable/human constant antibody. (GenScript USA Inc., Piscataway,  
461 NJ). Heavy and light cloned plasmids were mixed 1:1 and transfected into Expi293 cells  
462 according to manufacture protocol (ThermoFisher). Supernatants were harvested five  
463 days later and purified on protein A/G Hi-Trap columns on an AKTA FPLC (Cytiva).  
464 Antibody was eluted off the columns at low pH and dialyzed against 1xPBS. Antibody  
465 quantitation was performed by 280/260 absorbance on a Nanodrop spectrophotometer  
466 (DeNovix).

467

#### 468 **Histopathology and tissue immunofluorescence**

469 Mice lungs were perfused with 8 mL PBS and inflated with 0.7 mL of OCT compound  
470 (Tissue-Tek) mixed 1:1 v/v with 4% paraformaldehyde (Electron Microscopy Sciences)  
471 diluted in PBS. Inflated lungs were snap-frozen and stored at -80°C until sectioning.  
472 Tissue sections (4 µm) were stained with hematoxylin and eosin, and chronic lung  
473 disease was scored on a scale of 0 to 3 for alveolitis, peribroncholitis and airway  
474 metaplasia. Percentage values and area affected was determined, multiplied by the  
475 intensity scores previously defined, and the resulting weighted scores were graphed. For  
476 immunostaining analysis, tissue sections were washed in PBS to remove OCT, and Fc  
477 receptor blockade was performed using anti-mouse Fc $\gamma$ RIII/II (FcBlock) (Jackson  
478 Immunoresearch) diluted 1:200 in PBS containing 1% bovine serum albumin (BSA).  
479 Surface staining was performed using a panel of antibodies targeting T cells, B cells,  
480 macrophages, and dendritic cells (**Supplementary Table 1**) at 4°C overnight. Sections  
481 were washed in PBS and surface antibodies were detected with anti-Rat AlexaFluor-488

482 secondary antibody (BioLegend). After surface staining, sections were permeabilized with  
483 0.2% Saponin (Sigma) diluted in PBS containing 1% BSA and FcBlock (1:200), and  
484 intracellular staining was performed using recombinant hu-mouse anti SeV-NP antibody  
485 conjugated with AlexaFluor-647 (1:1000) (Invitrogen) in combination with either anti-Krt5  
486 (1:500) (BioLegend) or anti-Krt8 (1:200) for 1 h at room temperature. Intracellular primary  
487 antibodies were detected with anti-Rabbit AlexaFluor 488 or anti-Rat AlexaFluor 488  
488 secondary antibodies. Nuclear staining was performed with Hoechst (Invitrogen) and  
489 tissue autofluorescence was quenched using 1 x True Black (Biotium) diluted in 70%  
490 ethanol. Slides were mounted with Fluormount-G (Invitrogen) and images were acquired  
491 using a Zeiss Axio observer Widefield fluorescence microscope, using 5x and 20x  
492 objectives.

493

#### 494 **Fluorescence RNA *in situ* hybridization**

495 RNA *in situ* hybridization was performed using RNAscope Multiplex Fluorescent Reagent  
496 Kit v2 (Advanced Cell Diagnostics, Inc., Newark, NJ, USA) according to the  
497 manufacturer's instructions. Lung sections (4  $\mu$ m) were washed as described in the  
498 previous paragraph and hybridized for 2 h at 40°C with the RNAscope probe V-SeV-NP-  
499 C1 (Cat. No. 1118511-C1) targeting the genomic RNA sequence of NP gene.  
500 Preamplifier, amplifier, HRP-labeled oligos, and TSA plus (Cyanine3 or Cyanine5) (Akoya  
501 biosciences) dye was then hybridized at 40°C. Nuclear staining was performed with DAPI,  
502 and images were acquired as described in the previous sub-session.

503

#### 504 **Multicolor flow cytometry and cell sorting**

505 At 3 and 49 dpi, mouse lungs were inflated with 0.7 mL of digestion mix containing  
506 collagenase A (Sigma), dispase (Thermofisher), liberase TL (Sigma) and DNase I  
507 (Sigma) and incubated at 37°C for 30 min with agitation. Digested samples were then  
508 briefly vortexed and filtered through a 70-µm filter mesh to obtain single-cell suspensions.  
509 The obtained cells were washed with PBS containing 5% FBS, treated with red blood  
510 cells lysis buffer (Sigma), and total viable cells were quantified with trypan blue staining  
511 using an automated cell counter (TC-20 Automated Cell Counter; BioRad). For each  
512 sample, 2x10<sup>6</sup> cells were resuspended in PBS supplemented with 1% BSA and 2 mM  
513 EDTA (Corning). Next, Fc receptor blockade and viability staining were simultaneously  
514 performed using Rat anti-mouse Fc $\gamma$ RIII/II (CD16/32; BD Biosciences) and ZombieNIR  
515 (BioLegend) for 10 min at room temperature. To define major cell subpopulations (**Fig**  
516 **S1**) we employed a panel of 16 antibodies (**Table S1**) to stain for surface markers. For  
517 intracellular staining of Sendai virus NP, cells were fixed/permeabilized with the FoxP3/  
518 Transcription Factor Staining Buffer Set (eBioscience) following manufacturer's  
519 guidelines, and incubated with recombinant hu-mouse anti-SeV NP antibody, conjugated  
520 with AlexaFluor-647 (Invitrogen) for 1h at 4°C.

521 To isolate specific lung cell populations with fluorescent activated cell sorting  
522 (FACS), surface staining was performed as mentioned above using a panel of lineage-  
523 specific markers (**Supplementary Table 1**). Live CD45<sup>+</sup>, Lineage<sup>-</sup>, Thy1.2<sup>+</sup> and sm13<sup>+</sup>  
524 cells were defined as ILC2s. Macrophages were obtained from the same single-cell  
525 suspensions mentioned above using the Anti-F4/80 MicroBeads UltraPure, mouse  
526 (Miltenyi Biotec) isolation kit. All flow cytometry experiments were performed using a  
527 Cytek Aurora spectral flow cytometer (Cytek Biosciences), with acquisition of at least

528 1x10<sup>6</sup> total events. FACS experiments were performed using a BD-FACS Aria-II. Data  
529 analysis was done using FlowJo V12 software (Tree Star Inc.).

530

### 531 **RNA-seq of sorted cells**

532 For both ILC2 and macrophages obtained from SeV-infected sm13 mice, and for tdTom<sup>+</sup>,  
533 tdTom<sup>+</sup>NP<sup>+</sup>, and negative cells obtained from rSeV-C<sup>eGFP-Cre</sup>-infected tdTom mice, total  
534 RNA was extracted from at least three cell pools per condition, using KingFisher APEX  
535 automated RNA Extraction and Purification system (ThermoFisher) according to the  
536 manufacturer's guidelines. Each ILC2 and Macrophage sample, as well as tdTom<sup>+</sup>,  
537 tdTom<sup>+</sup>NP<sup>+</sup>, and negative cell samples was a resulting pool of cells from 2 individual  
538 animals. Total cDNA libraries were prepared from 100 ng of starting RNA using TruSeq  
539 Total RNA Library Prep Kit, with subsequent Ribo-Zero Human/Mouse/Rat Sample Prep  
540 Kit following manufacturer's instructions. Libraries were run on Illumina NovaSeq 6000 to  
541 generate 150 bp, paired-end reads, resulting in 79-120 million reads per sample with an  
542 average Phred score of 35.75.

543

### 544 **Viral reads and host transcriptome analysis**

545 Sequencing adaptors were removed from the raw sequencing data using Cutadapt<sup>49</sup>.  
546 Trimmed reads were then mapped to the mouse transcriptome (Ensembl release 79,  
547 EnsDb.Mmusculus.v79) using Kallisto, with 60 bootstraps per sample<sup>50</sup>. Subsequent  
548 import and annotation of transcripts were done in R environment using the TxImport  
549 package<sup>51</sup>. Differentially expressed genes (DEGs) (p value < 0.05, fold change > 2)  
550 between pairwise comparisons were obtained by linear modeling and Bayesian statistics

551 using the VOOM function from the Limma package<sup>52</sup>. Gene Ontology (GO) analysis was  
552 done using the enrichGO function from the ClusterProfiler package<sup>53</sup> with a p value cut-  
553 off of 0.05. Gene Set Enrichment Analysis (GSEA) was performed using the Molecular  
554 Signatures Database (MSigDB) msigdb R package<sup>54</sup> including pathways found in the  
555 C2, C5 and H Mus Musculus gene collections<sup>55,56</sup>. Finally, reads mapping the mouse  
556 genome were removed from the trimmed dataset using Bowtie2 v2.4.1<sup>57</sup> and virus  
557 coverage was obtained using SAMtools v1.15<sup>58</sup> after aligning the non-host reads to the  
558 rSeV-C<sup>eGFP-Cre</sup> genome using Bowtie2. Virus coverage per sample was visualized using  
559 the ggplot2 R package<sup>59</sup>. All data analysis was performed in RStudio (v. 2023.06.0+421).  
560

### 561 **Statistical analysis**

562 Statistical significance was inferred using GraphPad Prism software version 9.0  
563 (GraphPad Software, San Diego, CA). For animal experiments, group size consisted of  
564 3-7 mice per group. The weight-loss curve was analyzed by calculating the area under  
565 the curve (AUC) from both groups and comparing them using student t-tests. One-way  
566 and Two-way analysis of variance (ANOVA) with either Holm-Sídák or Bonferroni post-  
567 test was used to estimate the statistical significance between conditions of the remaining  
568 experiments. P values <0.05 were considered significant.

569

### 570 **Data deposition**

571 Next generation sequencing raw data of SeV-52 and rSeV-C<sup>eGFP-Cre</sup> experiments  
572 described in Figs 3, 4, and 5 was deposited in SRA under accession number  
573 PRJNA1034107.

574

575 **Acknowledgements**

576 We thank J. Andrew Duty from the Center for Therapeutic Antibody Development, Drug  
577 Discovery Institute, Icahn School of Medicine, Mount Sinai, New York, NY, USA for the  
578 technical support in the generation of the SeV humanized antibody used in this study. We  
579 thank the Tissue Histology Core at the Center for Reproductive Health Sciences,  
580 Department of Obstetrics & Gynecology, Washington University School of Medicine, Saint  
581 Louis, MO, USA for all the support with the tissue sectioning and histologic staining. We  
582 also thank the Flow Cytometry & Fluorescent Activated Cell Sorting Core at the  
583 Department of Pathology & Immunology, Washington University School of Medicine,  
584 Saint Louis, MO, USA for the help with the cell sorting experiments.

585

586 This project was funded by NIH grants AI127832 and A137062, and the Washington  
587 University BJC Investigator program (to C.B.L), NIH grants HL148033, AI176660, and  
588 AI163640 (to S.J.V.D.), and the National Research Korea Award NRF-2020  
589 R1A6A3A03037855 (to D.-H.K).

590

591 **Declaration of interests**

592 The authors declare no competing interests.

593

594

595

596

597 **References**

598

599 1 Shi, T. *et al.* Global, regional, and national disease burden estimates of acute  
600 lower respiratory infections due to respiratory syncytial virus in young children in  
601 2015: a systematic review and modelling study. *The Lancet* **390**, 946-958 (2017).  
[https://doi.org/10.1016/S0140-6736\(17\)30938-8](https://doi.org/10.1016/S0140-6736(17)30938-8)

602 2 Wang, X. *et al.* Global burden of acute lower respiratory infection associated with  
603 human metapneumovirus in children under 5 years in 2018: a systematic review  
604 and modelling study. *Lancet Glob Health* **9**, e33-e43 (2021).  
[https://doi.org/10.1016/S2214-109X\(20\)30393-4](https://doi.org/10.1016/S2214-109X(20)30393-4)

605 3 Weinberg, G. A. *et al.* Parainfluenza Virus Infection of Young Children: Estimates  
606 of the Population-Based Burden of Hospitalization. *The Journal of Pediatrics* **154**,  
607 694-699 (2009). <https://doi.org/10.1016/j.jpeds.2008.11.034>

608 4 O'Brien, K. L. *et al.* Causes of severe pneumonia requiring hospital admission in  
609 children without HIV infection from Africa and Asia: the PERCH multi-country  
610 case-control study. *The Lancet* **394**, 757-779 (2019).  
[https://doi.org/10.1016/S0140-6736\(19\)30721-4](https://doi.org/10.1016/S0140-6736(19)30721-4)

611 5 Okomo, U., Idoko, O. T. & Kampmann, B. The burden of viral respiratory  
612 infections in young children in low-resource settings. *Lancet Glob Health* **8**, e454-  
613 e455 (2020). [https://doi.org/10.1016/S2214-109X\(20\)30037-1](https://doi.org/10.1016/S2214-109X(20)30037-1)

614 6 Chen, J. *et al.* Long term outcomes in survivors of epidemic Influenza A (H7N9)  
615 virus infection. *Scientific Reports* **7**, 1-8 (2017). <https://doi.org/10.1038/s41598-017-17497-6>

616 7 Taylor, M. S. *et al.* A Conserved Distal Lung Regenerative Pathway in Acute  
617 Lung Injury. *American Journal of Pathology* **188**, 1149-1160 (2018).  
<https://doi.org/10.1016/j.ajpath.2018.01.021>

618 8 Sapey, E. & Stockley, R. A. COPD exacerbations · 2: Aetiology. *Thorax* **61**, 250-  
619 258 (2006). <https://doi.org/10.1136/thx.2005.041822>

620 9 Sivakumaran, S., Alsallakh, M. A., Lyons, R. A., Quint, J. K. & Davies, G. A.  
621 Estimating the contribution of respiratory pathogens to acute exacerbations of

627                   COPD using routine data. *Journal of Infection* **86**, 233-238 (2023).  
628                   <https://doi.org/10.1016/j.jinf.2023.01.012>

629           10   Andreas, A., Doris, L., Frank, K. & Michael, K. Focusing on severe infections with  
630                   the respiratory syncytial virus (RSV) in adults: Risk factors, symptomatology and  
631                   clinical course compared to influenza A / B and the original SARS-CoV-2 strain.  
632                   *Journal of Clinical Virology* **161**, 105399-105399 (2023).  
633                   <https://doi.org/10.1016/j.jcv.2023.105399>

634           11   Wendorf, K. A. *et al.* Subacute Sclerosing Panencephalitis: The Devastating  
635                   Measles Complication That Might Be More Common Than Previously Estimated.  
636                   *Clinical Infectious Diseases* **65**, 226-232 (2017).  
637                   <https://doi.org/10.1093/cid/cix302>

638           12   Griffin, D. E. Measles virus persistence and its consequences. *Curr Opin Virol*  
639                   **41**, 46-51 (2020). <https://doi.org/10.1016/j.coviro.2020.03.003>

640           13   Deen, G. F. *et al.* Ebola RNA Persistence in Semen of Ebola Virus Disease  
641                   Survivors — Final Report. *New England Journal of Medicine* **377**, 1428-1437  
642                   (2015). <https://doi.org/10.1056/NEJMoa1511410>

643           14   Hoarau, J.-J. *et al.* Persistent Chronic Inflammation and Infection by  
644                   Chikungunya Arthritogenic Alphavirus in Spite of a Robust Host Immune  
645                   Response. *The Journal of Immunology* **184**, 5914-5927 (2010).  
646                   <https://doi.org/10.4049/jimmunol.0900255>

647           15   Stein, S. R. *et al.* SARS-CoV-2 infection and persistence in the human body and  
648                   brain at autopsy. *Nature* **612** (2022). <https://doi.org/10.1038/s41586-022-05542-y>

649           16   Greninger, A. L. *et al.* Human parainfluenza virus evolution during lung infection  
650                   of immunocompromised individuals promotes viral persistence. *Journal of*  
651                   *Clinical Investigation* **131** (2021). <https://doi.org/10.1172/JCI150506>

652           17   Owusu, D. *et al.* Persistent SARS-CoV-2 RNA Shedding without Evidence of  
653                   Infectiousness: A Cohort Study of Individuals with COVID-19. *Journal of*  
654                   *Infectious Diseases* **224**, 1362-1371 (2021). <https://doi.org/10.1093/infdis/jiab107>

655           18   Tabatabai, J. *et al.* Parainfluenza virus infections in patients with hematological  
656                   malignancies or stem cell transplantation: Analysis of clinical characteristics,

657 nosocomial transmission and viral shedding. *PLoS One* **17**, e0271756 (2022).  
658 <https://doi.org/10.1371/journal.pone.0271756>

659 19 Wang, J. H., Kwon, H. J. & Jang, Y. J. Detection of parainfluenza virus 3 in  
660 turbinete epithelial cells of postviral olfactory dysfunction patients. *Laryngoscope*  
661 **117**, 1445-1449 (2007). <https://doi.org/10.1097/MLG.0b013e318063e878>

662 20 McCarthy, M. K. & Morrison, T. E. Persistent RNA virus infections: do PAMPS  
663 drive chronic disease? *Current Opinion in Virology* **23**, 8-15 (2017).  
664 <https://doi.org/10.1016/j.coviro.2017.01.003>

665 21 Griffin, D. E. Why does viral RNA sometimes persist after recovery from acute  
666 infections? *PLOS Biology* **20**, e3001687-e3001687 (2022).  
667 <https://doi.org/10.1371/journal.pbio.3001687>

668 22 Garcia, G. L., Valenzuela, A., Manzoni, T., Vaughan, A. E. & López, C. B.  
669 Distinct Chronic Post-Viral Lung Diseases upon Infection with Influenza or  
670 Parainfluenza Viruses Differentially Impact Superinfection Outcome. *American*  
671 *Journal of Pathology* **190**, 543-553 (2020).  
672 <https://doi.org/10.1016/j.ajpath.2019.11.003>

673 23 Burke, C. W., Bridges, O., Brown, S., Rahija, R. & Russel, C. J. Mode of  
674 Parainfluenza Virus Transmission Determines the Dynamics of Primary Infection  
675 and Protection from Reinfection. *Plos Pathogens* **9** (2013).  
676 <https://doi.org/10.1371/journal.ppat.1003786>

677 24 Byers, D. E. *et al.* Long-term IL-33-producing epithelial progenitor cells in chronic  
678 obstructive lung disease. *J Clin Invest* **123**, 3967-3982 (2013).  
679 <https://doi.org/10.1172/JCI65570>

680 25 Wu, K. *et al.* Group 2 Innate Lymphoid Cells Must Partner with the Myeloid–  
681 Macrophage Lineage for Long-Term Postviral Lung Disease. *The Journal of*  
682 *Immunology* **205**, 1084-1101 (2020). <https://doi.org/10.4049/jimmunol.2000181>

683 26 Liang, H. E., Reinhardt, R. L., Bando, J. K., Sullivan, B. M., Ho, I. C. & Locksley,  
684 R. M. Divergent expression patterns of IL-4 and IL-13 define unique functions in  
685 allergic immunity. *Nat Immunol* **13**, 58-66 (2011). <https://doi.org/10.1038/ni.2182>

686 27 Van Dyken, S. J. *et al.* A tissue checkpoint regulates type 2 immunity. *Nat*  
687 *Immunol* **17**, 1381-1387 (2016). <https://doi.org/10.1038/ni.3582>

688 28 Wu, X. *et al.* BATF promotes group 2 innate lymphoid cell–mediated lung tissue  
689 protection during acute respiratory virus infection. *Science Immunology* **7** (2022).  
690 <https://doi.org/10.1126/sciimmunol.abc9934>

691 29 Xu, J. *et al.* Replication defective viral genomes exploit a cellular pro-survival  
692 mechanism to establish paramyxovirus persistence. *Nature Communications* **8**  
693 (2017). <https://doi.org/10.1038/s41467-017-00909-6>

694 30 Schuurhof, A. *et al.* Gene Expression Differences in Lungs of Mice during  
695 Secondary Immune Responses to Respiratory Syncytial Virus Infection. *Journal*  
696 of *Virology* **84**, 9584-9594 (2010). <https://doi.org/10.1128/jvi.00302-10>

697 31 Ravi, L. I. *et al.* A systems-based approach to analyse the host response in  
698 murine lung macrophages challenged with respiratory syncytial virus. *BMC*  
699 *Genomics* **14** (2013). <https://doi.org/10.1186/1471-2164-14-190>

700 32 Young, A. R. *et al.* Dermal and muscle fibroblasts and skeletal myofibers survive  
701 chikungunya virus infection and harbor persistent RNA. *PLoS Pathog* **15**,  
702 e1007993 (2019). <https://doi.org/10.1371/journal.ppat.1007993>

703 33 Buch, T. *et al.* A Cre-inducible diphtheria toxin receptor mediates cell lineage  
704 ablation after toxin administration. *Nature Methods* **2**, 419-426 (2005).  
705 <https://doi.org/10.1038/nmeth762>

706 34 Diallo, B. *et al.* Resurgence of Ebola Virus Disease in Guinea Linked to a  
707 Survivor With Virus Persistence in Seminal Fluid for More Than 500 Days. *Clin*  
708 *Infect Dis* **63**, 1353-1356 (2016). <https://doi.org/10.1093/cid/ciw601>

709 35 Nelson, A. N. *et al.* Association of persistent wild-type measles virus RNA with  
710 long-term humoral immunity in rhesus macaques. *JCI Insight* **5** (2020).  
711 <https://doi.org/10.1172/jci.insight.134992>

712 36 Keeler, S. P., Agapov, E. V., Hinojosa, M. E., Letvin, A. N., Wu, K. & Holtzman,  
713 M. J. Influenza A Virus Infection Causes Chronic Lung Disease Linked to Sites of  
714 Active Viral RNA Remnants. *The Journal of Immunology* **201**, 2354-2368 (2018).  
715 <https://doi.org/10.4049/jimmunol.1800671>

716 37 Zhang, Y. *et al.* Respiratory Enterovirus (like Parainfluenza Virus) Can Cause  
717 Chronic Lung Disease if Protection by Airway Epithelial STAT1 Is Lost. *J*  
718 *Immunol* **202**, 2332-2347 (2019). <https://doi.org/10.4049/jimmunol.1801491>

719 38 Kim, E. Y. *et al.* Persistent activation of an innate immune response translates  
720 respiratory viral infection into chronic lung disease. *Nat Med* **14**, 633-640 (2008).  
721 <https://doi.org/10.1038/nm1770>

722 39 Kim, W. K. *et al.* Deficiency of melanoma differentiation-associated protein 5  
723 results in exacerbated chronic postviral lung inflammation. *Am J Respir Crit Care  
724 Med* **189**, 437-448 (2014). <https://doi.org/10.1164/rccm.201307-1338OC>

725 40 Wang, X. *et al.* TLR3-Activated Monocyte-Derived Dendritic Cells Trigger  
726 Progression from Acute Viral Infection to Chronic Disease in the Lung. *J Immunol*  
727 (2021). <https://doi.org/10.4049/jimmunol.2000965>

728 41 Fonseca, W., Lukacs, N. W., Elesela, S. & Malinczak, C. A. Role of ILC2 in Viral-  
729 Induced Lung Pathogenesis. *Frontiers in Immunology* **12**, 1-11 (2021).  
730 <https://doi.org/10.3389/fimmu.2021.675169>

731 42 Heaton, N. S., Langlois, R. A., Sachs, D., Lim, J. K., Palese, P. & tenOever, B. R.  
732 Long-term survival of influenza virus infected club cells drives immunopathology.  
733 *J Exp Med* **211**, 1707-1714 (2014). <https://doi.org/10.1084/jem.20140488>

734 43 Hamilton, J. R., Sachs, D., Lim, J. K., Langlois, R. A., Palese, P. & Heaton, N. S.  
735 Club cells surviving influenza A virus infection induce temporary nonspecific  
736 antiviral immunity. *Proc Natl Acad Sci U S A* **113**, 3861-3866 (2016).  
737 <https://doi.org/10.1073/pnas.1522376113>

738 44 Wheeler, D. L., Athmer, J., Meyerholz, D. K. & Perlman, S. Murine Olfactory Bulb  
739 Interneurons Survive Infection with a Neurotropic Coronavirus. *J Virol* **91** (2017).  
740 <https://doi.org/10.1128/JVI.01099-17>

741 45 Dumm, R. E., Fiege, J. K., Waring, B. M., Kuo, C. T., Langlois, R. A. & Heaton,  
742 N. S. Non-lytic clearance of influenza B virus from infected cells preserves  
743 epithelial barrier function. *Nat Commun* **10**, 779 (2019).  
744 <https://doi.org/10.1038/s41467-019-08617-z>

745 46 Reuther, P. *et al.* Persistent RNA virus infection is short-lived at the single-cell  
746 level but leaves transcriptomic footprints. *Journal of Experimental Medicine* **218**  
747 (2021). <https://doi.org/10.1084/jem.20210408>

748 47 Heaton, N. S. Revisiting the concept of a cytopathic viral infection. *PLoS Pathog*  
749 **13**, e1006409 (2017). <https://doi.org/10.1371/journal.ppat.1006409>

750 48 Reed, L. J. M. & Muench, H. A simple method of estimating fifty percent  
751 endpoints. *American Journal of Hygiene* **27**, 493-497 (1938).

752 49 Martin, M. Cutadapt removes adapter sequences from high-throughput sequence  
753 reads. *EMBnet Journal*, 1-3 (2011). <https://doi.org/10.14806/ej.17.1.200>

754 50 Shi, W. A Bioconductor R pipeline for analysis of RNA-seq data. *Protocol*  
755 *Exchange* (2015). <https://doi.org/10.1038/protex.2015.039>

756 51 Soneson, C., Love, M. & Robinson, M. Differential analyses for RNA-seq:  
757 transcript-level estimates improve gene-level inferences [version 2; peer review:  
758 2 approved]. *F1000Research* **4** (2016).  
<https://doi.org/10.12688/f1000research.7563.2>

760 52 Ritchie, M. E. *et al.* limma powers differential expression analyses for RNA-  
761 sequencing and microarray studies. *Nucleic Acids Research* **43**, e47-e47 (2015).  
<https://doi.org/10.1093/nar/gkv007>

763 53 Yu, G., Wang, L. G., Han, Y. & He, Q. Y. clusterProfiler: an R package for  
764 comparing biological themes among gene clusters. *OMICS* **16**, 284-287 (2012).  
<https://doi.org/10.1089/omi.2011.0118>

766 54 Liberzon, A., Subramanian, A., Pinchback, R., Thorvaldsdóttir, H., Tamayo, P. &  
767 Mesirov, J. P. Molecular signatures database (MSigDB) 3.0. *Bioinformatics* **27**,  
768 1739-1740 (2011). <https://doi.org/10.1093/bioinformatics/btr260>

769 55 Ashburner, M. *et al.* Gene Ontology: tool for the unification of biology. *Nature*  
770 *Genetics* **25**, 25-29 (2000). <https://doi.org/10.1038/75556>

771 56 Liberzon, A., Birger, C., Thorvaldsdóttir, H., Ghandi, M., Mesirov, J. P. &  
772 Tamayo, P. The Molecular Signatures Database (MSigDB) hallmark gene set  
773 collection. *Cell Syst* **1**, 417-425 (2015). <https://doi.org/10.1016/j.cels.2015.12.004>

774 57 Langmead, B. & Salzberg, S. L. Fast gapped-read alignment with Bowtie 2. *Nat*  
775 *Methods* **9**, 357-359 (2012). <https://doi.org/10.1038/nmeth.1923>

776 58 Danecek, P. *et al.* Twelve years of SAMtools and BCFtools. *Gigascience* **10**  
777 (2021). <https://doi.org/10.1093/gigascience/giab008>

778 59 Wickham, H. *ggplot2: Elegant Graphics for Data Analysis*. (Springer, 2016).

779

780

781 **Figure 1. Viral antigens and RNA persist in mouse lungs after SeV-driven acute**  
782 **illness. A.** Timeline of the study design. Mice were inoculated with either phosphate-  
783 buffered saline (mock) or  $5 \times 10^4$  tissue culture infectious dose (TCID<sub>50</sub>) of SeV 52 per  
784 animal. Lungs were analyzed on days 3 and 49 post-infection. **B.** Disease progression  
785 was monitored by measuring weight loss through the experiment. Data are representative  
786 of 4 independent experiments (mean  $\pm$  SD). For SeV-infected and mock groups the area  
787 under the curve (AUC) was calculated and t-tests were performed for statistical  
788 significance analysis. \*\*\*\*P<0.0001. **C.** Whole lung homogenates were harvested at days  
789 3 and 49 post-infection and both SeV NP RNA expression and infectious virus titers were  
790 quantified by qPCR and infectivity assays respectively. Relative RNA quantitation by  
791 qPCR was normalized to mouse GAPDH and  $\beta$ -Actin. Two-way analysis of variance with  
792 Holm-Sídák post-test was used to estimate statistical significance between groups. N = 5  
793 animals per group. \*P<0.05; \*\*P<0.01; \*\*\*\*P<0.0001. **D.** SeV-infected lungs were stained  
794 for SeV NP (white staining, upper panels) using immunofluorescence and for SeV NP  
795 RNA using RNAscope (white staining, lower panels). Nuclear staining (Hoechst for  
796 immunofluorescence and DAPI for RNAscope) in blue. Representative images of 3  
797 independent experiments. Scale bars: 100  $\mu$ m. **E.** SeV-infected lungs were stained for  
798 basal stem cells (Krt5<sup>+</sup>, green staining) and SeV NP (magenta staining) to localize SeV  
799 NP<sup>+</sup> cells in relation to areas displaying chronic lesions (dashed areas, subpanels E1-E3)  
800 and unaffected areas (subpanel E4). Arrowheads indicate SeV NP<sup>+</sup> cells, more detailed  
801 in the correspondent zoomed inset panels. Images were taken using a widefield  
802 microscope. Left panel, tiling image, 5x magnification. Right subpanels, 20x  
803 magnification. Right insets: digital zooms from the correspondent 20x magnification

804 images. Scale bars: Left panel. 500  $\mu$ m; Subpanels. 100  $\mu$ m. Images are representative  
805 of 3 independent experiments, 5 mice per group.

806

807 **Figure 2. Diverse lung immune cells express SeV NP during chronic infection. A.**  
808 Characterization of immune cells expressing SeV NP from cryopreserved mouse lungs  
809 after 49 dpi by immunofluorescence. Tissue sections were stained for SeV NP (magenta)  
810 in combination with the surface markers CD3 (T lymphocytes), CD11c, CD11b (dendritic  
811 cell subsets), F4/80 (macrophages), and Thy1.2 (Innate Lymphoid Cells and some T  
812 lymphocyte subsets) in green and red. Nuclear staining is displayed in blue. White arrows  
813 indicate individual SeV NP<sup>+</sup> cells. Images were taken in a widefield fluorescence  
814 microscope using a 20x magnification scope. Scale bars: 25  $\mu$ m. Representative images  
815 from three independent experiments, 5 mice per condition. Right panels: insets from the  
816 dashed areas. **B-E.** Lungs from SeV-infected mice were harvested at 3 and 49 dpi,  
817 enzymatically digested, and analyzed by multiplex spectral flow cytometry with a panel of  
818 16 antibodies to quantify **(B and C)** and characterize **(D and E)** SeV<sup>+</sup> cells. **B.**  
819 Representative dot plots of SeV NP<sup>+</sup> cells (% of live) comparing acute (3 dpi) with long-  
820 term (49 dpi) SeV infection. SeV NP<sup>+</sup> gates were drawn based on the isotype control and  
821 the mock-infected samples. **C.** Frequency of SeV NP<sup>+</sup> cells gated on total live cells from  
822 SeV 3 days-, SeV 49 days-, and mock-infected lungs. **D.** Representative histograms of  
823 SeV NP<sup>+</sup> fluorescence intensity from 9 individual cell subsets, B cells, ILC2s, T CD4<sup>+</sup>  
824 lymphocytes, T CD8<sup>+</sup> lymphocytes, NK cells, Polymorphonuclear cells (PMNs), Alveolar  
825 macrophages (AMs), Tissue macrophages (TMs), and Dendritic cells (DCs) at 49 dpi.  
826 Histograms from SeV-infected animals are displayed in red while histograms from mock-

827 infected animals are displayed in gray. **E**. Frequency and mean fluorescence intensity  
828 (MFI) of SeV NP<sup>+</sup> cells within lymphoid- and myeloid-origin cell subsets. All multiple  
829 comparisons were done with one-way ANOVA and Holm-Sídák post-test. \*P<0.05;  
830 \*\*P<0.01; \*\*\*P<0.0005; \*\*\*\*P<0.0001. Data representative of two independent  
831 experiments, 4-5 animals per condition, total 1 million events acquired per animal.

832

833 **Figure 3. Type 2 innate lymphoid cells and macrophages are persistently activated**  
834 **in a type 2 inflammation manner during SeV chronic lung disease.** Lung type 2 innate  
835 lymphoid cells (ILC2s) (**A-C**), and macrophages (**D-F**) were isolated either from SeV- or  
836 mock-infected mouse lungs after 49 dpi and subjected to bulk RNA-seq. **A** and **D**. Volcano  
837 plots indicating differentially expressed genes detected in ILC2s and macrophages,  
838 respectively, from SeV-infected lungs over mock. P<0.05, LogFC>2. **B-C**. Scattered dot  
839 plots showing expression of ILC2 hallmark genes (**B**) and virus-related ISGs (**C**). Each  
840 dot corresponds to an individual pool of cells (n = 6 animals pooled in pairs per condition).  
841 **E-F**. Scattered dot plots indicating expression of Th2 polarization (**E**) and phagocytic  
842 activity (**F**) genes from macrophages. Each dot corresponds to cells obtained from an  
843 individual animal (minimum n = 3 animals per condition). Data are displayed as mean ±  
844 SD. Two-way analysis of variance (ANOVA) with Bonferroni post-test was used to  
845 estimate statistical significance between multiple comparisons. \*P<0.05; \*\*P<0.01;  
846 \*\*\*\*P<0.0001. CPM, copies per million. **G**. Bubble chart showing gene set enrichment  
847 analysis (GSEA) of upregulated genes in ILC2s and macrophages sorted from SeV 49  
848 dpi lungs. Bubble size indicates gene set size per GSEA pathway, while bubble color  
849 gradient indicates Normalized Enrichment Scores (NES) values.

850

851 **Figure 4. Paramyxovirus infection clearance is not complete and leaves long-term**  
852 **survivor cells in the lower respiratory tract expressing persistent viral RNA and**  
853 **viral proteins. A.** B6.Cg-Gt(ROSA)<sup>tdTom</sup> (tdTom) mice were inoculated intranasally with  
854 either PBS (mock) or 5x10<sup>5</sup> TCID<sub>50</sub> rSeV-C<sup>e</sup>GFP-C<sup>re</sup>. Lungs were harvested at 3, and 49 dpi  
855 for flow cytometry (FC) analysis, and cell sorting at 49 dpi. Weight loss was recorded up  
856 to 21 dpi to monitor disease progression. Data (mean±SD) are representative of 2  
857 individual experiments (minimum 3 mice per group). **B.** Representative dot plots  
858 comparing percentage of tdTom<sup>+</sup> cells in mouse lungs during acute (3 dpi) and chronic  
859 (49 dpi) rSeV- C<sup>e</sup>GFP-C<sup>re</sup> infection. **C.** Frequency of tdTom<sup>+</sup> cells gated on total live cells  
860 from rSeV-C<sup>e</sup>GFP-C<sup>re</sup> 3 days-, rSeV- C<sup>e</sup>GFP-C<sup>re</sup> 49 days-, and mock-infected lungs. Data are  
861 shown as mean±SD. Statistical significance was estimated with one-way ANOVA using  
862 Bonferroni post-test. \*\*\*P<0.005. **D-E.** Characterization of immune (CD45<sup>+</sup>) and non-  
863 immune (CD45<sup>-</sup>) cell proportions within tdTom<sup>+</sup> cells. Representative dot plots (**D**) and  
864 quantification (**E**) of CD45 staining in tdTom<sup>+</sup> cells during acute (3 dpi) and chronic (49  
865 dpi) rSeV-C<sup>e</sup>GFP-C<sup>re</sup> infection. Statistical significance was estimated with two-way ANOVA  
866 and Holm-Sídák post-test. \*P<0.05. **F.** Combination of tdTom and SeV NP detection  
867 enables sorting of two distinct subsets of VID cells, SeV-infected cells persistently  
868 expressing viral antigens (tdTom<sup>+</sup>NP<sup>+</sup>) and SeV-infected/survivor cells only (tdTom<sup>+</sup>NP<sup>-</sup>).  
869 Representative dot plots indicating the gating strategy used for sorting 3 cell  
870 subpopulations from rSeV-C<sup>e</sup>GFP-C<sup>re</sup>-infected lungs tdTom<sup>+</sup>NP<sup>-</sup>, tdTom<sup>+</sup>NP<sup>+</sup>, and negative.  
871 Negative cells from mock-infected lungs were also sorted. Data representative of 2  
872 individual experiments, 6 mice per condition. **G.** Sorted cells were pooled (2 mice) and

873 subjected to RNAseq. Normalized viral reads per  $10^8$  total reads are displayed per  
874 individual pool of tdTom<sup>+</sup>NP<sup>-</sup> and tdTom<sup>+</sup>NP<sup>+</sup> cells. **H.** Coverage analysis indicating  
875 normalized viral reads per genome position in each individual cell pool. Viral specific gene  
876 regions and reporter genes are indicated in light gray.

877

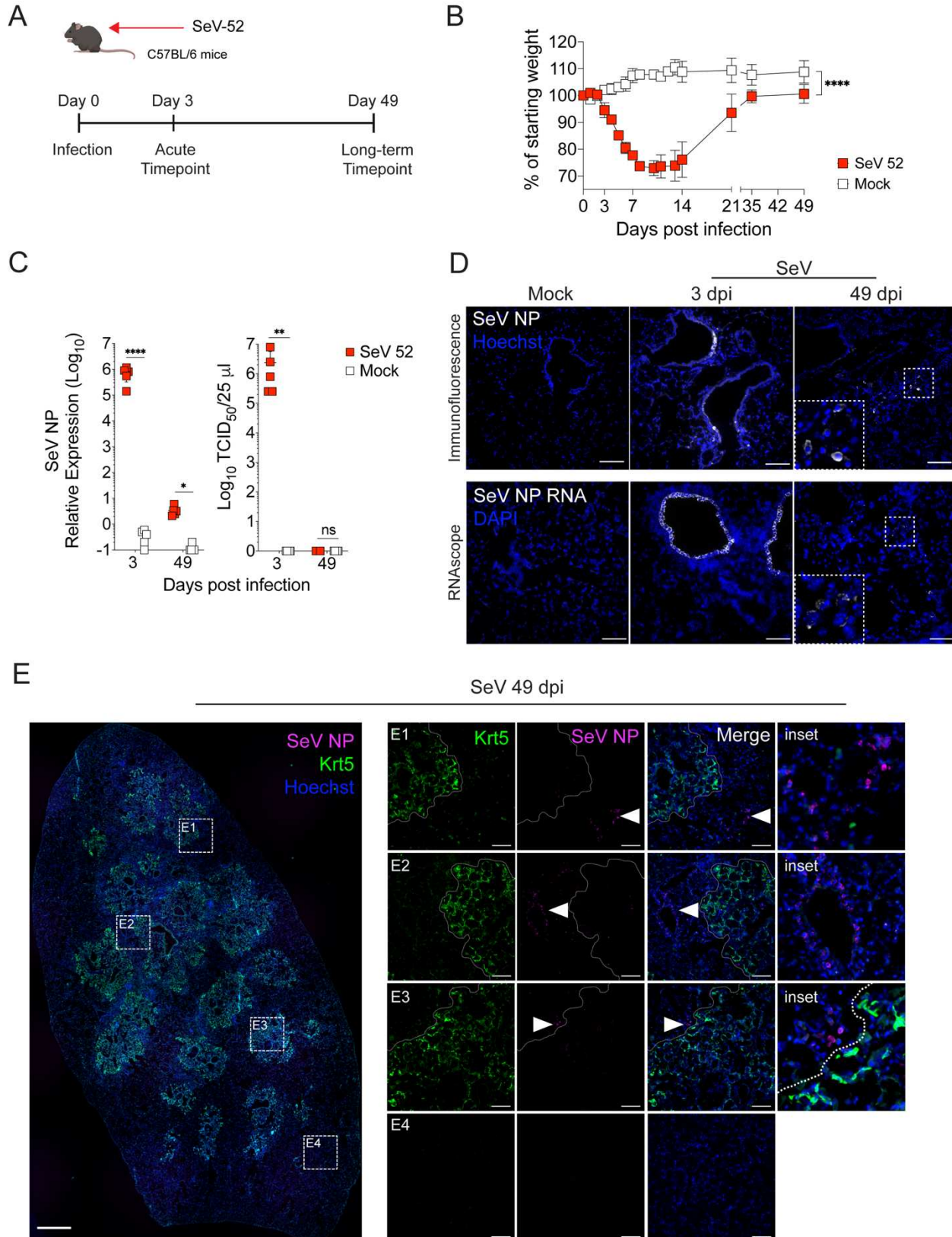
878 **Figure 5. Viral clearance and persistence entails opposing transcriptional**  
879 **programs in long-term SeV-infected lungs.** Viral infected and cells derived from them  
880 sorted from tdTom mice infected with rSeV-C<sup>eGFP</sup>Cre at 49 dpi were subjected to bulk  
881 RNAseq and host transcriptome analysis. **A.** Volcano plots indicating differentially  
882 expressed genes (DEGs) in tdTom<sup>+</sup>NP<sup>-</sup>, tdTom<sup>+</sup>NP<sup>+</sup>, and Negative cells against Mock  
883 negative cells. **B.** Venn diagram showing overlapping DEGs from tdTom<sup>+</sup>NP<sup>-</sup> and  
884 tdTom<sup>+</sup>NP<sup>+</sup>, as well as exclusive DEGs from each cell subset. **C.** Bar graphs showing  
885 gene ontology (GO) enrichment analysis of each of the VID cell subsets (tdTom<sup>+</sup>NP<sup>-</sup> and  
886 tdTom<sup>+</sup>NP<sup>+</sup>) exclusive DEGs. **D.** Heatmaps of selected gene collections from the GO  
887 pathways in **C.** Shown are fold change (FC) values of tdTom<sup>+</sup>NP<sup>-</sup> and tdTom<sup>+</sup>NP<sup>-</sup> are  
888 displayed. Columns groups are color-coded following the same patterns on **C.** and **B.** **E.**  
889 Gene set enrichment assay (GSEA) bubble chart indicating the most significant enriched  
890 pathways of tdTom<sup>+</sup>NP<sup>+</sup> transcriptome signatures in comparison with tdTom<sup>+</sup>NP<sup>-</sup> cells.  
891 Bubble color gradient indicates Normalized enrichment score (NES), and bubble sizes  
892 correspond to gene set size on each pathway.

893

894 **Figure 6. Chronic lung pathology induced by paramyxovirus infection is dependent**  
895 **on long-term surviving and persistently infected cells. A.** Diphtheria toxin regime

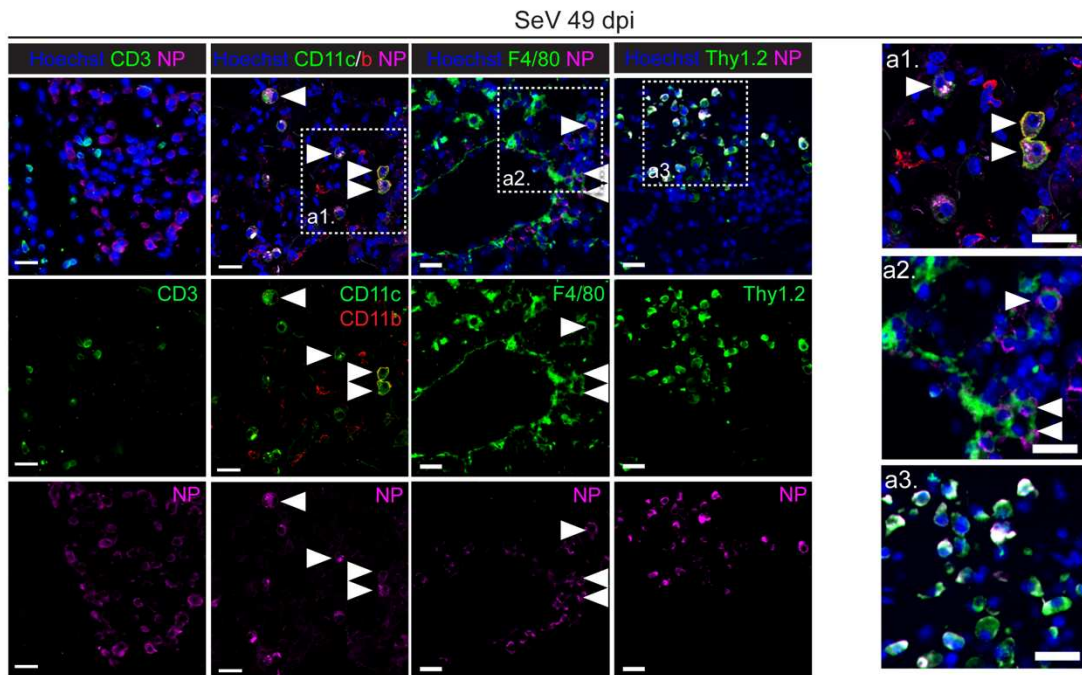
896 treatment and timepoints for tissue harvesting and analysis. **B.** Disease progression was  
897 assessed by monitoring animal weight loss until 26 dpi. Graphs are representative of 2  
898 independent experiments and depict mean weight loss values  $\pm$ SD, 4 mice per condition.  
899 **C.** Mouse lungs were harvested at 49 dpi and tissue sections were stained with  
900 Hematoxylin and Eosin to compare pathological changes between the analysis groups.  
901 Top panels indicate representative images of whole lung sections (Brightfield, 5x  
902 magnification tiled images, Scale bars: 1 mm) and bottom panels indicate zoomed-in  
903 images from the indicated areas (Brightfield, 5x magnification tiled images, scale bars:  
904 100  $\mu$ m). 4 animals per condition. **D.** Lung sections from SeV +DT and SeV -DT groups  
905 were blindly scored for histopathological changes. Total area affected, percentage of  
906 airway structures affected, and intensity of alveolitis, peribroncholitis, and bronchus-  
907 associated lymphoid tissue (BALT) expansion were determined for every individual lung  
908 sample. Individual weighted scores values  $\pm$ SD are indicated. Data representative of 2  
909 individual experiments, 4-7 mice per condition. **E.** Lung sections were stained for the  
910 tissue remodeling and chronic lung lesion markers Krt5 (green) and Krt8 (magenta) with  
911 immunofluorescence to check for chronic lung lesion progression. Nuclear staining is  
912 displayed in blue. The dashed area indicates chronic lung lesions and areas of intense  
913 tissue remodeling. Images were taken with a widefield microscope. Upper panels, tiling  
914 images, 20x magnification, scale bars: 500  $\mu$ m. Lower panels: 20x magnification, scale  
915 bars: 100  $\mu$ m. **F.** Quantification of chronic lung lesion area (%) over total lung section  
916 area. Mean values  $\pm$ SD are shown. Data are representative of two individual experiments,  
917 4-7 mice per condition. Statistical significance was estimated using one-way ANOVA and  
918 Bonferroni post-test. \*P<0.05.

919 **Figure 1.**  
920

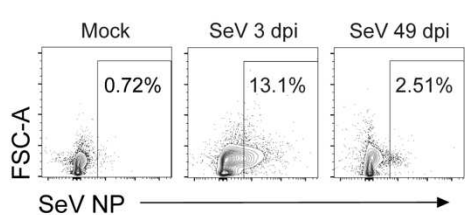


922 **Figure 2.**  
923

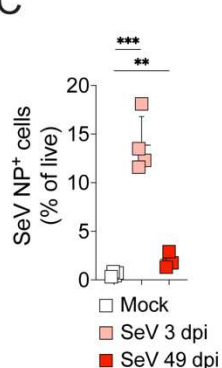
A



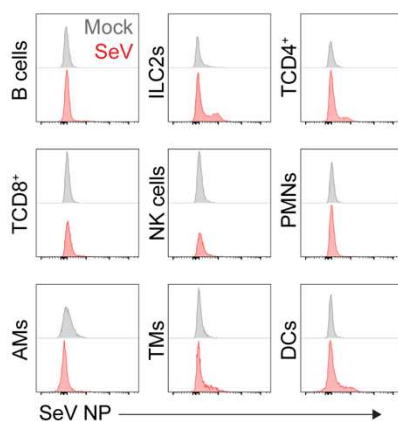
B



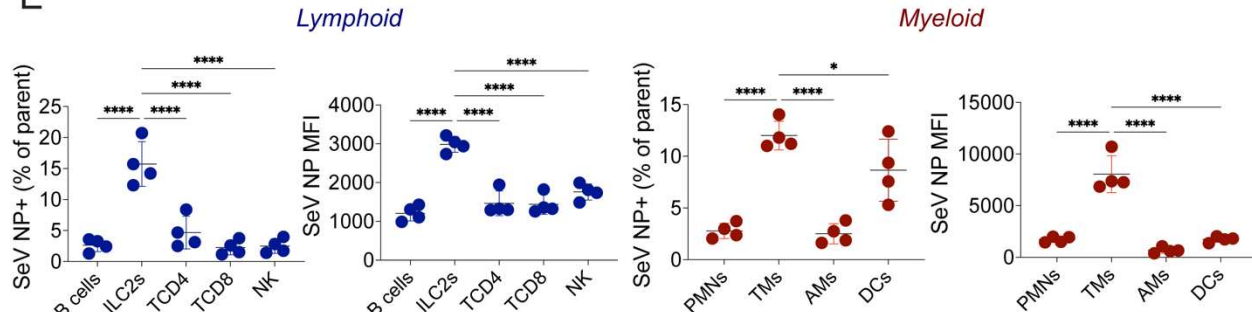
C



D



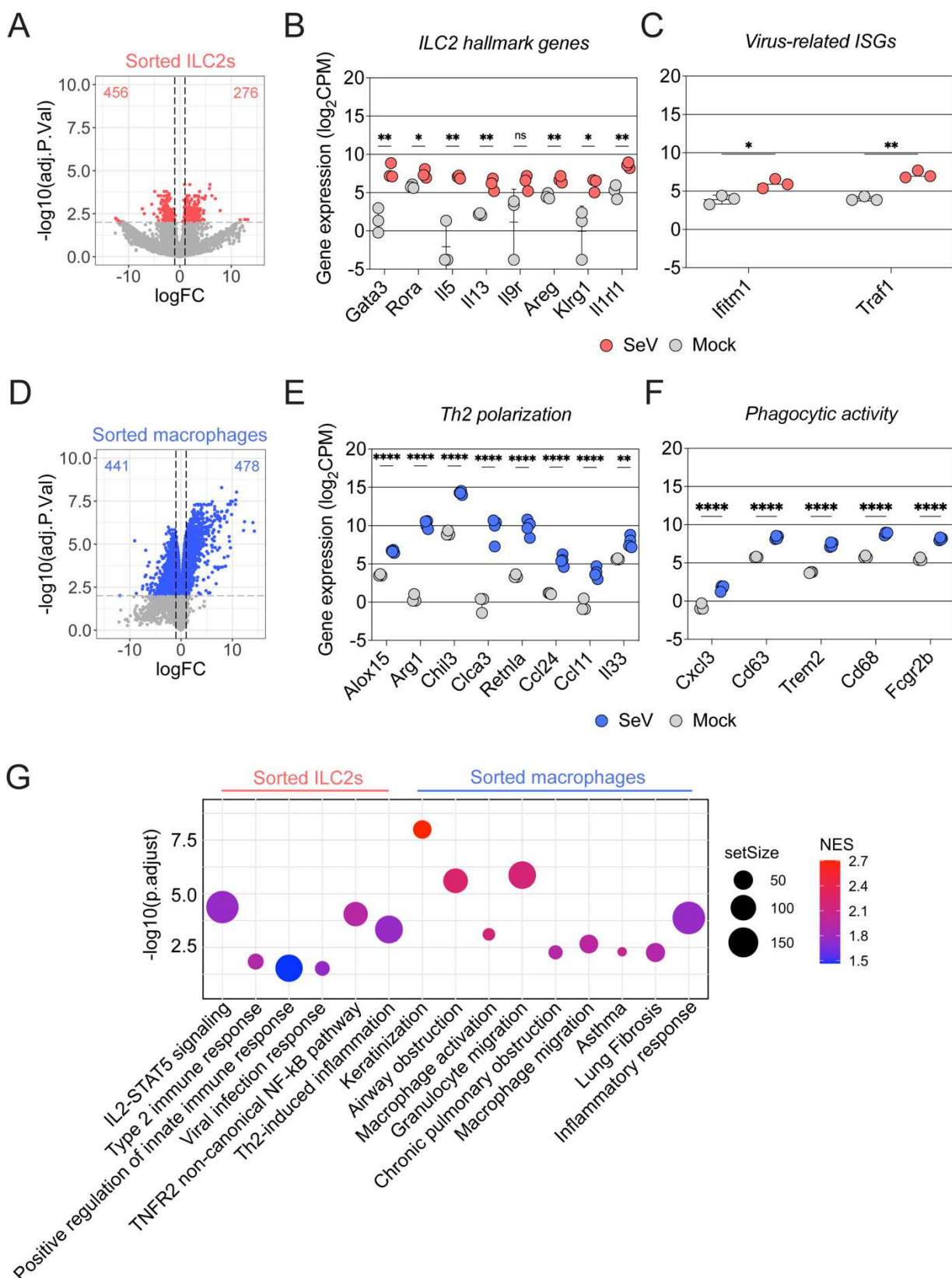
E



924  
925  
926  
927  
928

929  
930

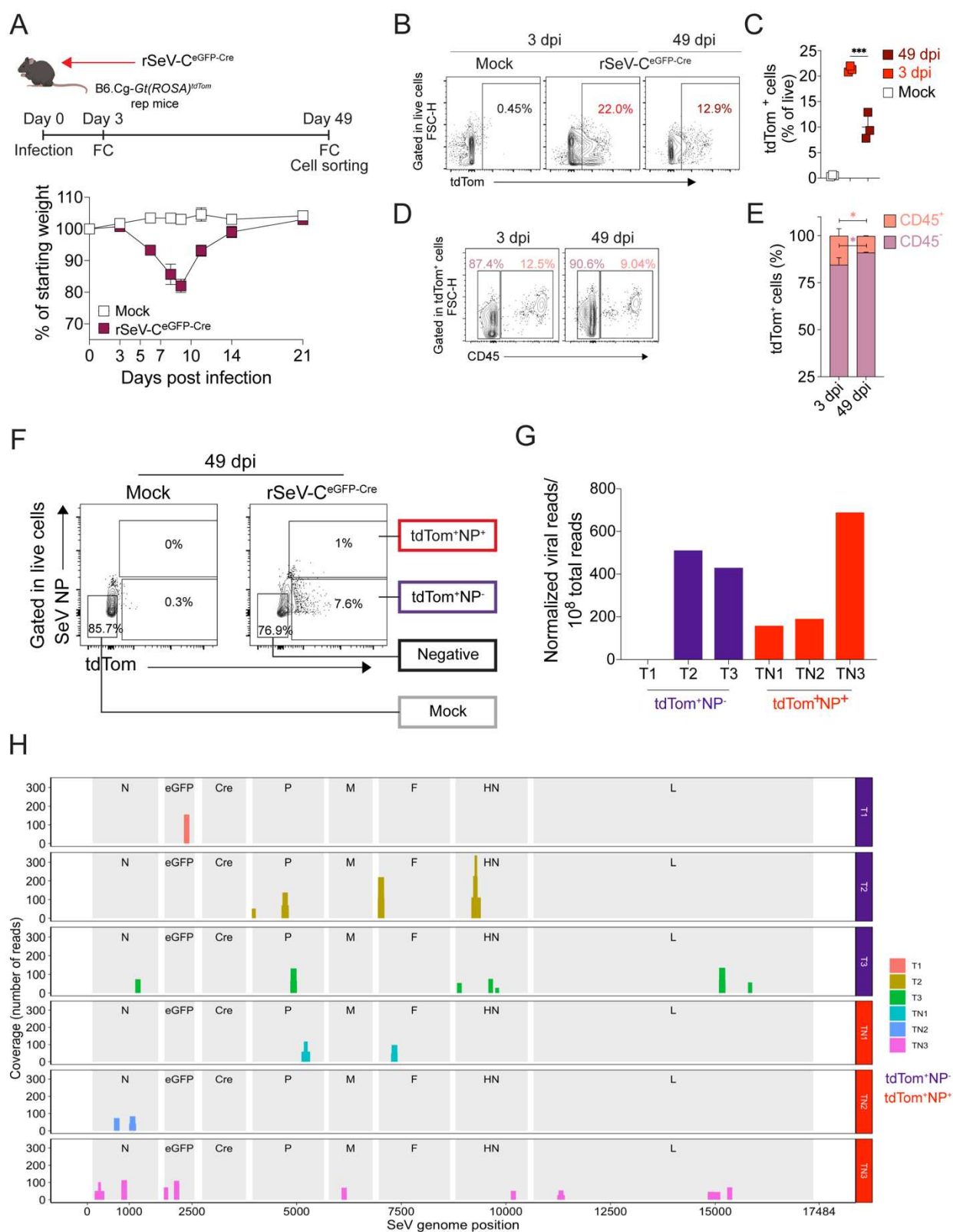
**Figure 3.**



931

932 **Figure 4.**

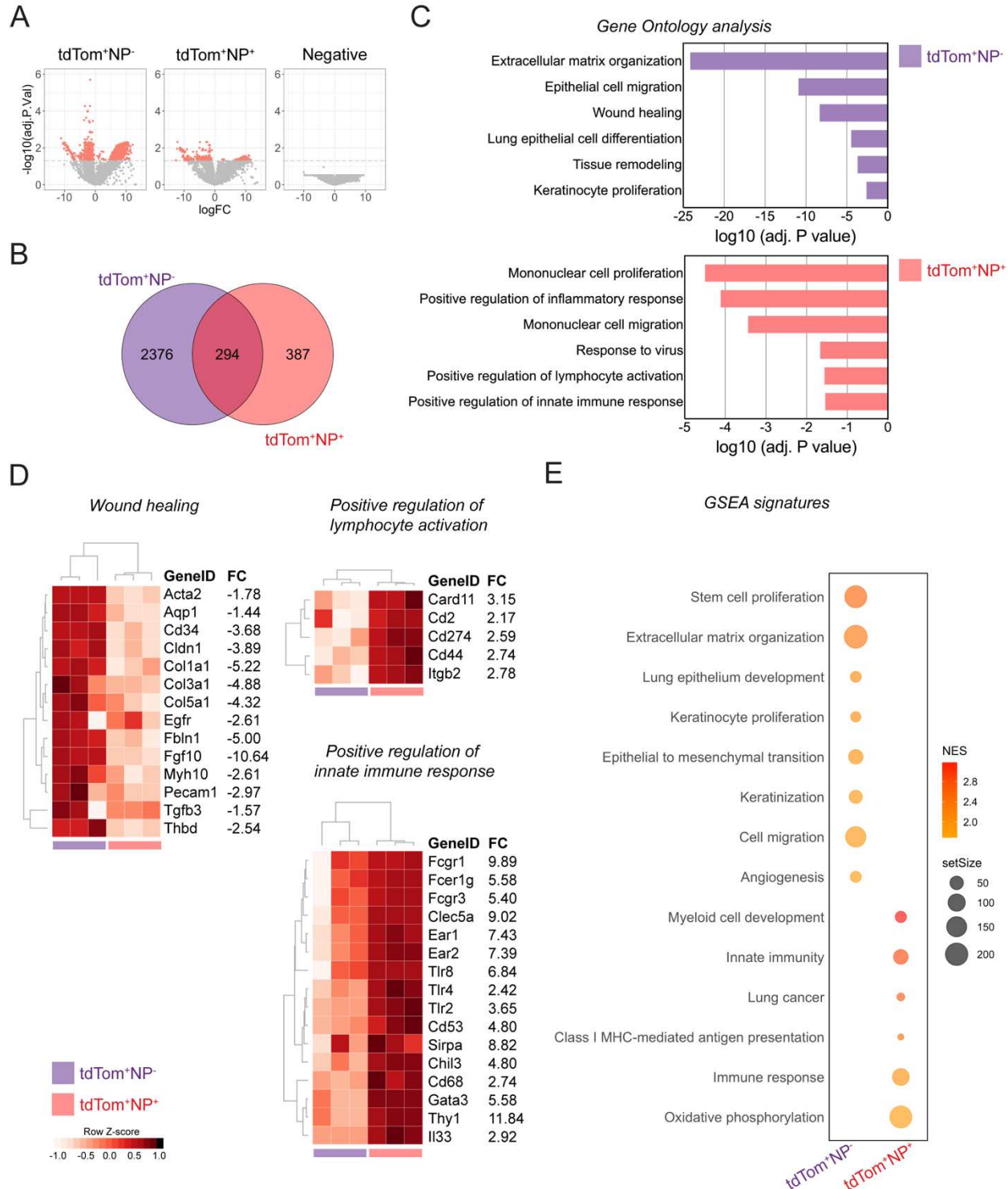
933



934

935

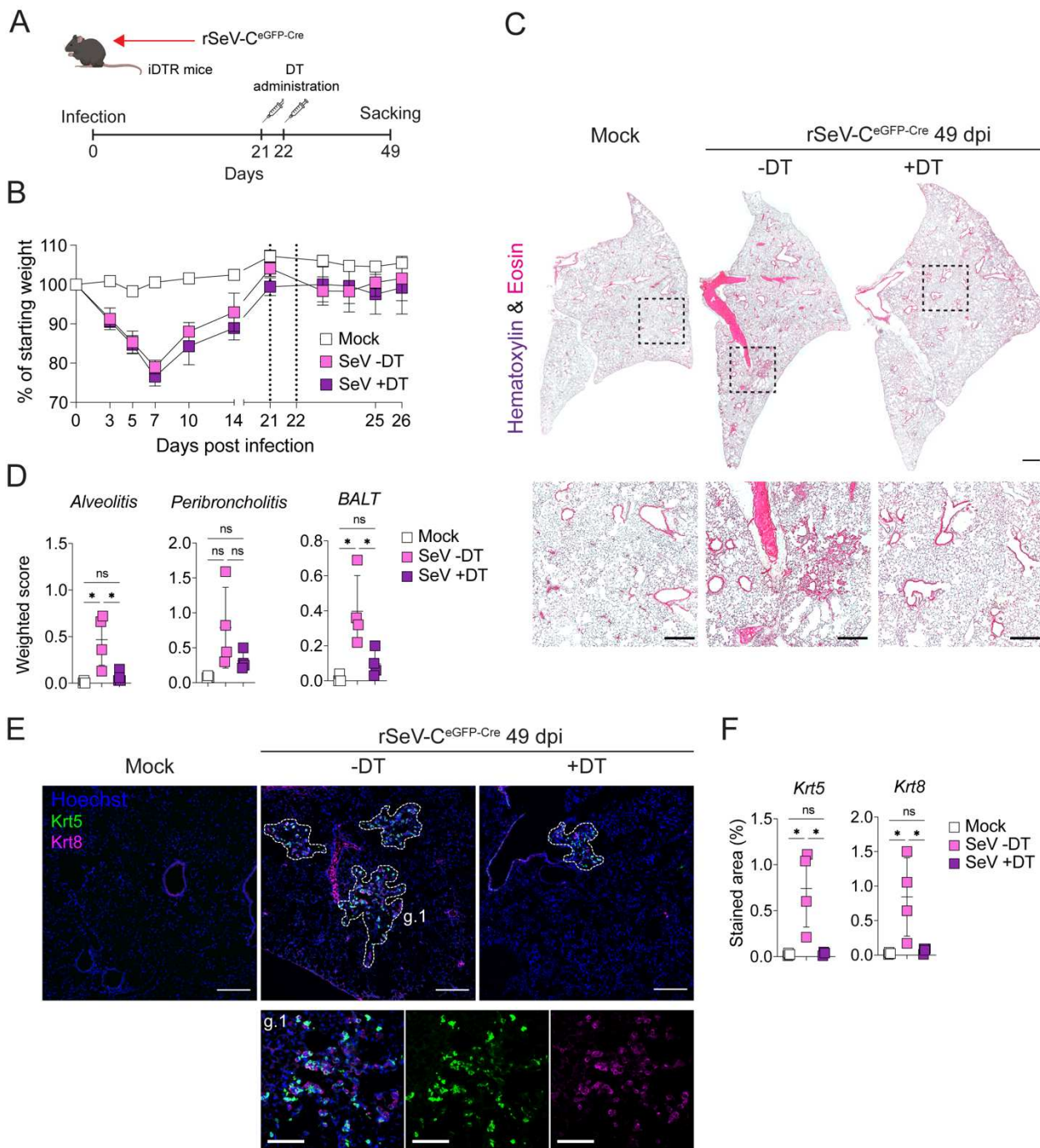
936 **Figure 5.**  
937



938  
939  
940  
941  
942

943 **Figure 6.**

944

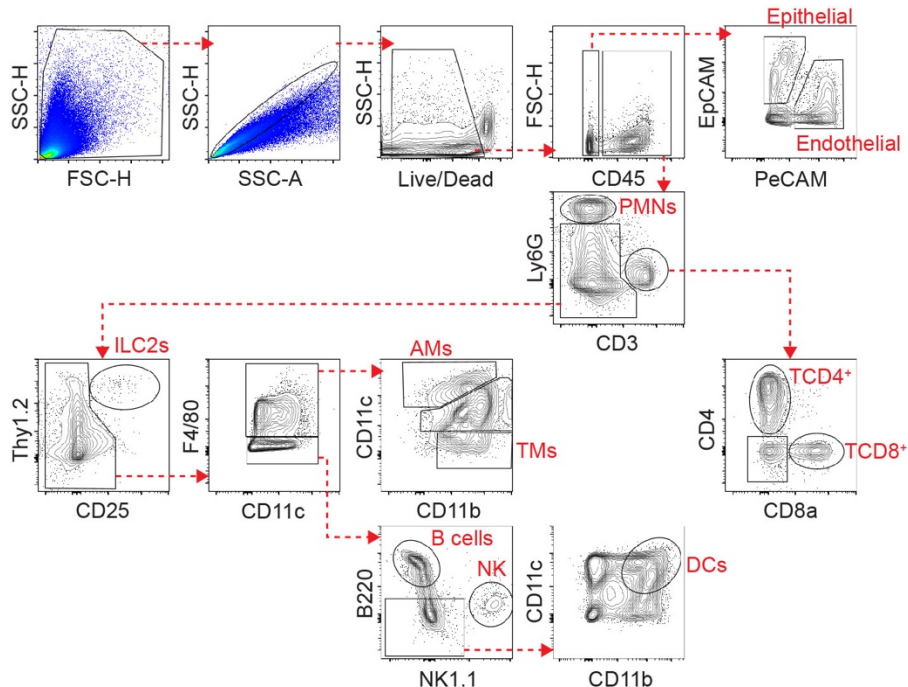


945  
946

947

948

949

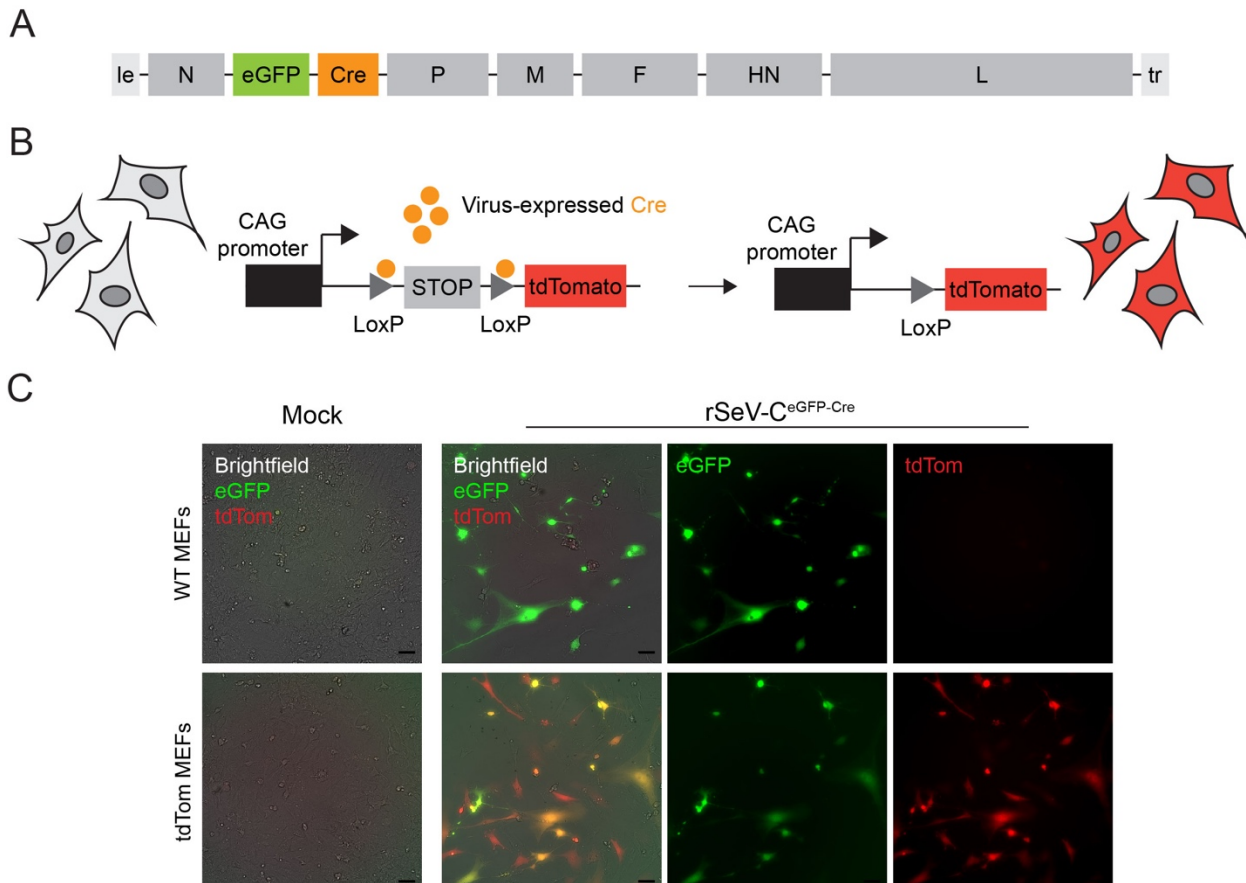


950  
951

**Figure S1. Gating strategy for spectral flow cytometry analysis of SeV-infected lungs.**

952 Representative dot plots indicating the following cell subsets defined from live cells: Epithelial  
953 cells ( $CD45^- EpCAM^+ PeCAM^+$ ), Endothelial cells ( $CD45^- EpCAM^+ PeCAM^+$ ), Polymorphonuclear  
954 cells (PMNs) ( $CD45^+ Ly6G^+ CD3^-$ ), T CD4 $^+$  lymphocytes ( $CD45^+ Ly6G^- CD3^+ CD4^+ CD8a^-$ ), T CD8 $^+$   
955 lymphocytes ( $CD45^+ Ly6G^- CD3^+ CD4^- CD8a^+$ ), Type 2 innate lymphoid cells (ILC2s) ( $CD45^+ Ly6G^-$   
956  $CD3^- Thy1.2^+ CD25^+$ ), Alveolar macrophages (AMs) ( $CD45^+ Ly6G^- CD3^- F4/80^+ CD11c^{hi} CD11b^{low}$ ),  
957 Tissue macrophages (TMs) ( $CD45^+ Ly6G^- CD3^- F4/80^+ CD11c^{low} CD11b^{hi}$ ), B cells ( $CD45^+ Ly6G^-$   
958  $CD3^- F4/80^- B220^{hi}$ ), Natural killer cells (NK) ( $CD45^+ Ly6G^- CD3^- F4/80^- B220^- NK1.1^{hi}$ ), Dendritic cells  
959 (DCs) ( $CD45^+ Ly6G^- CD3^- F4/80^- B220^- NK1.1^- CD11c^{hi} CD11b^{hi}$ ).  
960

961  
962  
963  
964  
965  
966  
967  
968  
969  
970  
971  
972  
973  
974  
975  
976  
977  
978  
979

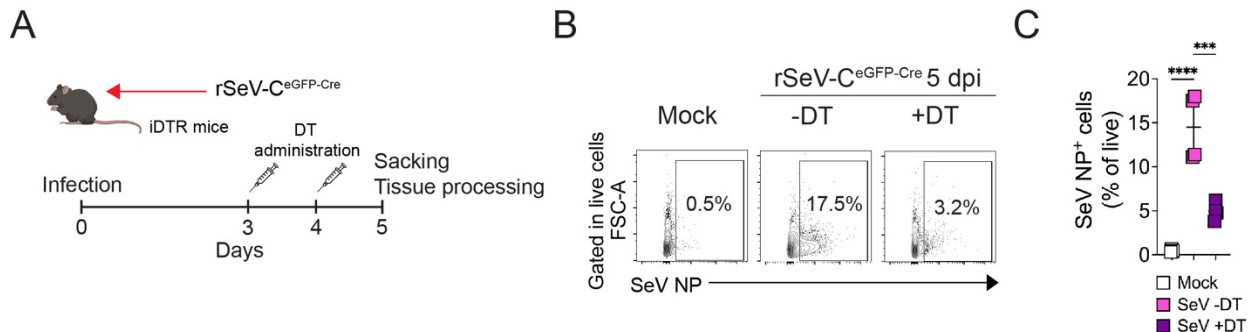


980  
981  
982  
983  
984

**Figure S2. Generation of a Cre-expressing recombinant Sendai virus. A.** Genome schematics showing the insertion of eGFP and the recombinase Cre genes as independent reading frames in the SeV Cantell genome, between the virus genes N and P, to generate a Cre-expressing SeV recombinant virus (rSeV-C<sup>eGFP-Cre</sup>). **B.** Schematic design showing Cre recombination of the LoxP-STOP-tdTomato reporter gene cassette leading to constitutive expression of the tdTomato fluorescent protein. **C.** Murine embryonic fibroblasts (MEFs) from either WT C57BL/6 mice or tdTomato reporter mice were infected *in vitro* at a multiplicity of infection (MOI) of 0.01 TCID<sub>50</sub>/cell to test the robustness of the reporter system. Representative images from two independent experiments were taken after 24 hpi using a widefield fluorescence microscope. eGFP signal (green) and tdTomato signal (red) were overlaid on brightfield images of WT and tdTomato-infected MEFs. 20x magnification. Scale bars: 50  $\mu$ m.

996  
997  
998  
999  
1000  
1001  
1002  
1003

1004



1005

1006

1007 **Figure S3. Diphtheria toxin administration efficiently depletes SeV infected cells. A.**  
1008 Experimental design showing diphtheria toxin (DT) regime treatment and timepoints for tissue  
1009 harvesting and analysis. **B.** Representative dot plots of rSeV-CeGFP-Cre -infected lungs analyzed  
1010 by flow cytometry for SeV NP expression. 50,000 events acquired. **C.** Quantification of SeV NP<sup>+</sup>  
1011 cell frequency (% of live) detected by flow cytometry at 5 dpi. Mean values ±SD are displayed,  
1012 data are representative of 2 individual experiments, 4-5 mice per group. One way ANOVA with  
1013 Bonferroni post-test was used to estimate statistical significance between groups. \*\*\*P<0.0005,  
1014 \*\*\*\*P<0.0001.

1015

1016

1017

1018

1019

1020

1021

1022

1023

1024

1025

1026

1027

1028

1029

1030

1031

1032

1033

1034

1035

1036

1037

1038

1039

1040

1041

1042

1043 **Table S1. Key reagents**

1044

Reagent	Company	Catalog N.
<b>Antibodies</b>		
Anti-mouse EpCAM (CD326) BV421 antibody	Biolegend	118225
Anti-mouse Ly6G eFluor450 antibody	eBioscience	48-5931-82
Anti-mouse CD8a BV570 antibody	Biolegend	100740
Anti-mouse PeCAM (CD31) BV605 antibody	Biolegend	102427
Anti-mouse CD4 BV711 antibody	Biolegend	100447
Anti-mouse F4/80 BV785 antibody	Biolegend	123141
Anti-mouse Thy1.2 (CD90.2) AlexaFluor 488 antibody	Biolegend	105316
Anti-mouse NK1.1 BB700 antibody	BD Biosciences	566502
Anti-mouse B220 PerCP-eFluor 710 antibody	eBioscience	46-0452-82
Anti-mouse CD25 PE antibody	eBioscience	12-0251-81
Anti-mouse CD64 PE-Cy5 antibody	Thermofisher	MA5-38711
Anti-mouse CD11c PE-Cy7 antibody	eBioscience	25-0114-82
Anti-mouse CD11b AlexaFluor 700 antibody	BD Pharmingen	557960
Anti-mouse CD45.2 APC-eFluor 780 antibody	eBioscience	47-0454-82
Anti-mouse CD3 APC-Fire 810 antibody	Biolegend	100268
Anti-mouse CD11c FITC antibody	eBioscience	11-0114-85
Rabbit anti-mouse Krt5 antibody	Biolegend	905504
Rat anti-mouse Krt8 antibody	DSHB	TROMA-I
Rat anti-mouse CD3 antibody	BD Biosciences	555273
Rat anti-mouse F4/80 antibody	BD Biosciences	565409
Rat anti-mouse B220 antibody	BD Biosciences	553084
Rat anti-mouse Thy1.2 (CD90.2) antibody	Biolegend	140301
Rat anti-mouse CD16/CD32 (FcBlock)	Biolegend	101320
anti-mouse CD3 biotin-conjugated	Biolegend	309806
anti-mouse CD4 biotin-conjugated	Biolegend	100244
anti-mouse CD8a biotin-conjugated	Biolegend	100508
anti-mouse/human CD11b biotin-conjugated	Biolegend	11704
anti-mouse Ly6G/Ly6C (Gr-1) biotin-conjugated	Biolegend	101204
anti-mouse NK1.1 biotin-conjugated	Biolegend	108403
anti-mouse CD49b (Pan-NK) biotin-conjugated	Biolegend	108704
anti-mouse CD19 biotin-conjugated	Biolegend	108903
anti-mouse Ter-119 (Erythroid cells) biotin-conjugated	Biolegend	115504
anti-mouse CD11c biotin-conjugated	Biolegend	116203
anti-mouse TCR gamma/delta biotin-conjugated	Biolegend	117304
anti-mouse CD170 (Siglec-F) biotin-conjugated	Biolegend	118103
anti-mouse CD90.2 (Thy1.2) Antibody biotin-conjugated	Biolegend	155512
anti-human CD4 Antibody biotin-conjugated	Biolegend	140314
Goat Anti-Rabbit AlexaFluor488 Secondary antibody	Invitrogen	A-11008
Anti-Rat AlexaFluor488 Secondary antibody	Biolegend	405418
Goat Anti-Rat AlexaFluor647 Secondary antibody	Invitrogen	A-21247
<b>Commercial assays</b>		
RNAscope® Multiplex Fluorescent Detection Kit v2	ACD	323110
RNAscope® Target Retrieval Reagents	ACD	322000
RNAscope® 2.5 HD Detection Reagents-BROWN	ACD	322310
TSA Plus Fluorescein Kit 50-150 slides	Akoya biosciences	NEL741001KT
TSA Plus Cyanine 3 Kit 50-150 slides	Akoya biosciences	NEL744001KT
TSA Plus Cyanine 5 Kit 50-150 slides	Akoya biosciences	NEL745001KT
Power SYBR™ Green PCR Master Mix	ThermoFisher	4367660
High Capacity cDNA Reverse Transcription Kit	Applied Biosystems	4368813

Zombie NIR™ Fixable Viability Kit	Biolegend	423106
AlexaFluor 647 Antibody Labeling kit	ThermoFisher	A20186
<b>General reagents</b>		
BSA	Sigma	A3059-100G
TPCK-treated Trypsin	Worthington Biochem. Corporation	#LS003750
EDTA	Corning	46-034-CI
DNAse I (for molecular biology)	ThermoScientific	#EN0252
Paraformaldehyde (PFA)	Electron Microscopy Sciences	15714-5
Saponin	Sigma	47036-50G-F
Collagenase A	Sigma	10103586001
Dispase	Gibco	17105-041
Liberase TL	Sigma	5401020001
DNAse I (for tissue digestion)	Sigma	10104159001

1045